

# Self-Distillation of Hidden Layers for Self-Supervised Representation Learning

Scott C. Lowe<sup>1,\*</sup> Anthony Fuller<sup>1,2</sup> Sageev Oore<sup>1,3</sup>  
Evan Shelhamer<sup>1,4</sup> Graham W. Taylor<sup>1,5</sup>

<sup>1</sup>Vector Institute <sup>2</sup>Carleton University <sup>3</sup>Dalhousie University  
<sup>4</sup>University of British Columbia <sup>5</sup>University of Guelph

## Abstract

The landscape of self-supervised learning (SSL) is currently dominated by generative approaches (e.g., MAE) that reconstruct raw low-level data, and predictive approaches (e.g., I-JEPA) that predict high-level abstract embeddings. While generative methods provide strong grounding, they are computationally inefficient for high-redundancy modalities like imagery, and their training objective does not prioritize learning high-level, conceptual features. Conversely, predictive methods often suffer from training instability due to their reliance on the non-stationary targets of final-layer self-distillation. We introduce **Bootleg**, a method that bridges this divide by tasking the model with predicting latent representations from *multiple hidden layers* of a teacher network. This hierarchical objective forces the model to capture features at varying levels of abstraction simultaneously. We demonstrate that Bootleg significantly outperforms comparable baselines (+10% over I-JEPA) on classification of ImageNet-1K and iNaturalist-21, and semantic segmentation of ADE20K and Cityscapes.

## 1 Introduction

Large-scale pretraining using self-supervised learning (SSL) is an incredibly powerful representation learning technique, able to efficiently use large volumes of unlabelled data, and is thus used in many domains and applications. The most powerful image SSL methods at present are contrastive, such as DINOv3 (Siméoni et al., 2025) and Franca (Venkataramanan et al., 2025), requiring multiple views derived from domain-specific data augmentation and interactions between samples within the batch, resulting in tremendous computational resources being needed to fit large batches in memory (e.g. the smallest Franca training is distributed across 32 H100 GPUs). Among single-view and batch-size-independent methods, MAE (He et al., 2022) and I-JEPA (Assran et al., 2023) remain SOTA and are widely used, e.g., in video (Wang et al., 2023; Bardes et al., 2024; Assran et al., 2025), audio (Huang et al., 2022; Fei et al., 2024; Tuncay et al., 2025; Yuksel et al., 2025), remote sensing (Cong et al., 2022; Fuller et al., 2022), medical imaging (Zhou et al., 2023; Xiao et al., 2023), 3D point clouds (Zhang et al., 2022; Chen et al., 2023), time series (Nie et al., 2023; Li et al., 2023), DNA modelling (Safari et al., 2025), multimodal data (Bachmann et al., 2022; Chen et al., 2025; Lei et al., 2025), and more (Dong et al., 2024; Riou et al., 2024; Thimonier et al., 2025; Hachana & Rasheed, 2025). These methods are more computationally accessible (in only needing smaller batches) and general (in not requiring specific augmentations). However, both have their own disadvantages. MAE builds a representation learning model out of a generative modelling task, resulting in embeddings which are useful in pixel-space, but are less capable of representing high-level features. Consequently, MAE pretrained models require fine-tuning to be useful for downstream tasks, and cannot reasonably be used without fine-tuning. On the other hand, I-JEPA relies on *last layer* self-distillation, which is less stable to train because the targets are derived from the network we are training. This circularity means the training targets are less stimulus-driven/grounded, which can result in the model being detached from reality and collapsing during training. We thus introduce Bootleg, which learns superior representations by reconstructing *multiple hidden layers* in its own teacher-encoder.

## 2 Background: ViTs and masked modelling

**Vision transformers.** ViTs (Dosovitskiy et al., 2021) split images into patches:  $\mathbb{R}^{R \times R \times C} \rightarrow \mathbb{R}^{N \times P \cdot P \cdot C}$ , where  $N$  is the number of patches,  $P$  is the patch size,  $R$  is the image height and width, and  $C$  is the number of channels.

\*Correspondence: scott.lowe@vectorinstitute.ai

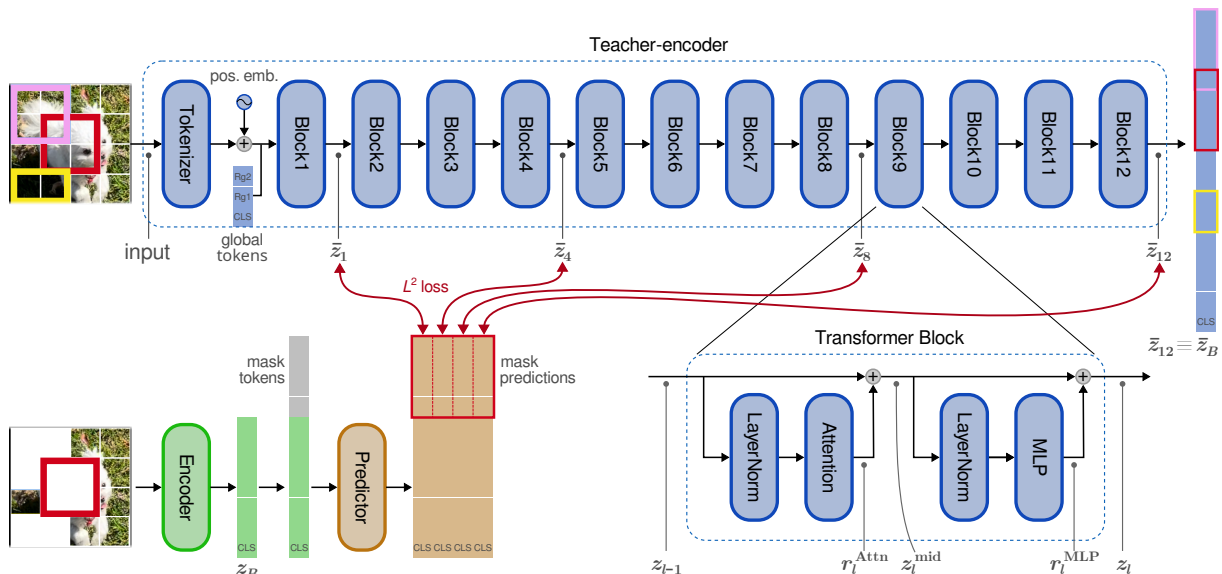


Figure 1: Multi-layer self-distillation with Bootleg. The teacher-encoder (blue), student-encoder (green), and predictor (orange) are ViTs, made of repeated transformer blocks. A schematic of a single transformer block is overlaid (bottom right). The teacher-encoder is an EMA of the student-encoder, and processes the full image. The student-encoder sees a subset of the image and must create embeddings of them to facilitate the predictor. The predictor processes the embeddings to predict representations at multiple layers within the teacher-encoder.

Patches are then projected to the model embedding dimension  $D$  with positional embeddings added to make “patch tokens”:  $x \in \mathbb{R}^{N \times P \times C} \rightarrow z^{\text{patch}} \in \mathbb{R}^{N \times D}$ . ViTs then optionally prepend  $G$  global tokens (class and register tokens (Darcet et al., 2024)) and process the token embeddings with  $B$  blocks:  $z_0 := (z^{\text{glob}}, z^{\text{patch}})$  and  $z_{l+1} = \text{Block}_l(z_l)$ , where  $z_l \in \mathbb{R}^{(G+N) \times D}$  is the feature map after the  $l$ -th block. Each block is comprised of a self-attention sub-block and a two-layer perceptron (MLP) sub-block, each of which adds to the representation through a residual connection:  $r_l^{\text{Attn}} := \text{Attn}_l(\text{LN}(z_{l-1}))$ ,  $z_l^{\text{mid}} := z_{l-1} + r_l^{\text{Attn}}$ ,  $r_l^{\text{MLP}} := \text{MLP}_l(\text{LN}(z_l^{\text{mid}}))$ , and  $z_l := z_l^{\text{mid}} + r_l^{\text{MLP}}$ . ViTs can efficiently process a sparse subset of patches via “masking”, in which a subset of the  $N$  patch tokens are dropped according to a masking strategy. Masking significantly decreases computational costs since the masked-out tokens (and their self-attentive interactions with the other tokens) do not need to be processed; this pairs well with “fill-in-the-blank” style pretraining algorithms such as those we consider here.

**MAE and I-JEPA.** The masked autoencoder (MAE) and image-based joint-embedding predictive architecture (I-JEPA) are popular methods for pretraining that rely on masking for self-supervised learning. Both methods train a model comprised of a ViT encoder and predictor, trained end to end. Most image patches (around 75%) are masked-out, and the remaining unmasked/visible patches are given to the encoder to produce visible-patch embeddings,  $z_B^{\text{vis}}$ . The visible-patch embeddings are concatenated with mask embeddings,  $m^{\text{mask}}$ , that represent the hidden-patch locations—these act as placeholders to be updated with the decoder’s prediction. In MAE, the model’s training objective is to predict the *pixels* of the hidden patches (target =  $x^{\text{mask}}$ ); whereas in I-JEPA, the models target the *final embeddings* of the hidden patches (target =  $z_B^{\text{mask}}$ ). I-JEPA’s target embeddings are computed by processing the full image with a teacher-encoder model, which follows the (student) encoder by using an exponential moving average (EMA) of its weights. Conceptually, this choice of *target* is the key difference between MAE and I-JEPA. Yet, as we will demonstrate, there are several implementation details that are also crucial. For example, MAE samples masks uniformly at random, whereas I-JEPA uses a more involved masking strategy where four contiguous rectangular regions are masked out.

**Data2vec.** Data2vec (Baevski et al., 2022, 2023) uses a similar training methodology to MAE and I-JEPA with self-distillation. Its target is the mean of instance-norm standardized vectors from the final  $K$  layers of the teacher, with the implicit assumption that representations across a large section of the network can be linearly integrated together. With a focus on efficient training, its predictor is a small convolutional module and each pass through the teacher module is accompanied with 16 passes through the student encoder-predictor with different randomly sampled masks.

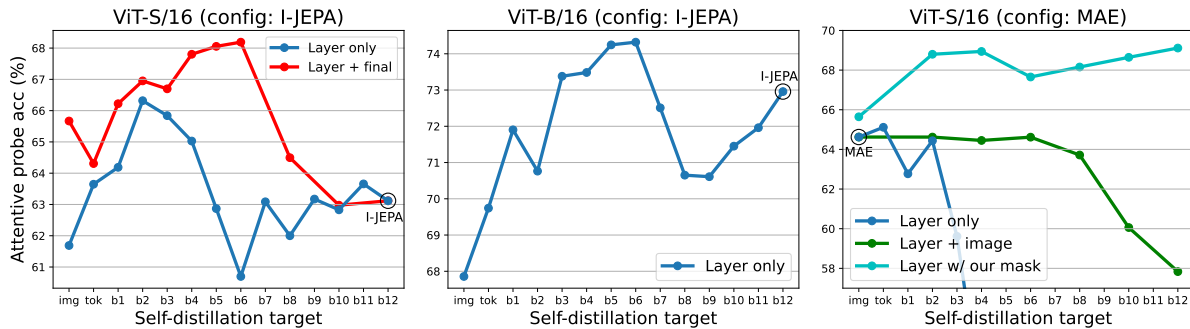


Figure 2: Bridging I-JEPA and MAE with targets across hidden layers. *Left:* We train ViT-S with I-JEPA, except for the target which we change to be a hidden layer ( $x$ -axis) of the teacher-encoder instead of its final output (blue curve) or in addition to the final output (red). We plot the frozen attentive probe top-1 accuracy on IN-1k ( $y$ -axis) for the respective encoders. *Middle:* Similar, but for ViT-B to verify at larger scale. *Right:* We train ViT-S using MAE, except we add EMA for self-distillation and change the target to be a hidden layer of the EMA model instead of the input pixels (blue) or in addition to the image pixels (green). We compare to a single target with our masking strategy (cyan). In all cases, self-distillation of a hidden target is able to improve on predicting only the input or the output.

### 3 Motivation for hidden targets

#### 3.1 Intuition: abstraction, tasks, and stability

**Deeper embeddings are more abstract.** The abstraction level of representations generally increases with increasing network depth. Image models receive pixels, which are the lowest level of abstraction, as their input and transform them layer-by-layer into features that are more useful for the task. Models tend to represent “low-level” features in early layers (*e.g.*, colours, edges, and textures) and “high-level” features in deep layers (*e.g.*, objects and semantic concepts). This has been observed for CNNs (Zeiler & Fergus, 2014; Bau et al., 2017; Zhou et al., 2015) and ViTs (Raghu et al., 2021; Vilas et al., 2023) trained with supervised learning or various SSL algorithms (Park et al., 2023; Lepori et al., 2024). Similarly, other work has found that hidden representations in CNNs and ViTs are correlated with the visual hierarchy in human brains, with early layers of the network best correlated with activity in the primary visual cortex that represents low-level features (oriented edges) and subsequent layers correlated with activity in progressively higher-level brain regions (Yamins et al., 2014; Yamins & DiCarlo, 2016; Horikawa & Kamitani, 2017; Tang et al., 2025; Raugel et al., 2025). Our training approach can be seen as analogous to a predictive coding model of the brain (Rao & Ballard, 1999; Friston, 2005; Friston & Kiebel, 2009; Clark, 2013; Keller & Mscis-Flogel, 2018; Nejad et al., 2025)—if we view the embeddings at masked locations as being desynchronous forward propagations of the same stimulus, the neurons corresponding to seen locations aim to predict the afferent representations which are about to be received from all layers to which they are connected.

**Deepest may not be best.** The layer with the most useful features depends on the pretraining and downstream tasks. For example, the abstraction level can increase, peak, then decrease across layers for ViTs pretrained to predict masked *pixels* (Park et al., 2023), in which case we may want to target a specific hidden layer to maximize the abstraction level of our target. And even if the final layer is the most abstract, mid-level embeddings are more useful for many tasks (Bolya et al., 2025; Evci et al., 2022). All of these studies consider *trained* models, and their findings can directly inform distillation from a frozen teacher. Conversely, we pretrain from scratch via self-distillation, which makes choosing the target layer more complex: the optimal choice may change throughout pretraining and create feedback effects that influence which layers become most useful. To avoid committing to a specific hidden layer, our Bootleg predictor simultaneously targets early, mid, and deep embeddings, “using the whole buffalo”.

**Stability.** Self-distillation methods are known to be unstable, whereas MAE is reliable because it targets pixels, which prevent destructive feedback. For example, slight changes to I-JEPA’s masking strategy results in  $>10\%$  decreases in accuracy (Assran et al., 2023). By targeting the teacher’s embeddings at various depths (*e.g.*, early, middle, and late), we include targets that are minimally processed (*i.e.*, by fewer layers) and hence are more stimulus-driven, providing grounding to the training objective, which helps prevent degenerate solutions to the task.

**Information bottleneck.** Our training objective can also be viewed through the lens of information compression. We task the model with predicting latent representations of the stimulus at multiple levels (*e.g.*  $|L| = 4$ ) of

abstraction, with a total of  $|L| \times |M| \times D$  target elements, but the encoder must pass this information to the predictor through a bottleneck sized  $1 \times |N| \times D_{\text{pred}}$ , with  $|N| < |M|$  and  $D_{\text{pred}} < D$  since the majority of tokens are masked out and the predictor network is narrower than the encoder. By increasing  $|L|$ , we increase the bottleneck ratio and hence increase the amount of compression it must perform, which is only possible if it understands the stimulus sufficiently well (Tishby et al., 1999). Moreover, note that there can be redundancy across both the embedding dimension ( $D$ ), sequence dimension ( $M$ ) and the target layers ( $L$ ). Intuitively, such correlations can cause collapse during training if the entropy of the targets is smaller than the size of the bottleneck, but (1) there is less correlation across the sequence dimension for early layers in the network (Park et al., 2023; Raghu et al., 2021) and (2) by training the model to self-distil multiple levels of abstraction into its own output layer, we ask it to compress the information from all these levels into the space of a single layer, repeatedly.

### 3.2 Illustrative experiments

As a proof-of-concept, we explore bridging the MAE and I-JEPA methods by simply sweeping the targets from the input layer (pixels) to the output layer (latents). Fig. 2 shows the results of training ViT-S with a basic, *i.e.*, ablated form of Bootleg: I-JEPA where the target is a layer of intermediate abstraction (a hidden layer within the teacher-encoder). We observe that it is superior to using the image or final embedding as the target, with the best self-distillation target being the output of the second layer of the teacher (left, blue line). A similar trend is seen for ViT-B (middle), where the best single target is the 6th layer. In both cases, the performance falls for deeper layers before rising again when the target is the output layer (12th layer). Furthermore, multiple targets (a hidden layer of the teacher-encoder concatenated with its final layer), even with the same predictor capacity, yields superior performance to using a single hidden target (left, red line).

When we train with MAE but change the prediction target to a hidden layer, we find that performance decreases, with the training instabilities causing a complete collapse in the model if the target is in the 4th layer or deeper (right, blue line). This issue is alleviated by predicting both the image pixels and a hidden layer (green line), which prevents the instabilities and model collapse. However, this is no better at the downstream task than predicting only pixels. Furthermore, we find that using the image pixels as one type of target amongst multiple levels of representation (*i.e.* when the weighting on the pixel reconstruction loss term is less than a quarter of the total loss) is insufficient to prevent collapse during training (not shown). When we change the masking strategy from uniform random to either I-JEPA’s masks (not shown) or Bootleg’s masks (cyan line), this sole change to the MAE is sufficient to stabilize training with hidden-self-distillation, and we observe a trend that is similar to the hidden-self-distillation version of I-JEPA (left).

## 4 Method

We now describe our hidden-self-distillation training method, Bootleg, illustrated in Fig. 1.

**Objective.** Given “seen” patches of an image, create high-level representations of these patches to predict the missing representations of “masked” patches, with targets selected from multiple levels of the layer hierarchy. Our methodology is most similar to I-JEPA (Assran et al., 2023), with the main conceptual difference being the expansion of the targets to multiple hidden layers, instead of only the final layer.

**Masking.** Our masking method is based on that of I-JEPA, with technical improvements in implementation as described in Appx. C, but without significant conceptual changes. For a given image, we split it into patches (of  $P \times P$  pixels), as per the ViT tokenizer. We randomly select a size and aspect ratio of rectangles to mask out, then randomly select the placement of four rectangular masks. These four masks, which may overlap, determine the missing representations that the student-encoder and predictor must learn to predict. Any unmasked patches (in the complement of the union of the masks) are the input for the student-encoder,  $z_0^{\text{vis}}$ .

**Targets.** The whole, unmasked, image is passed through a teacher-encoder. The teacher-encoder is a ViT with its weights an EMA of the student-encoder. For each of the masked locations, we collect the embeddings of the corresponding patch tokens outputted by certain ViT blocks within the teacher-encoder,  $\bar{z}_l$  for  $l \in L$ . The  $|L|$  target blocks are spread evenly across the depth of the encoder from the first transformer block to the final block, so as to maximize the diversity of embeddings used as targets. Specifically, we use every 4th block within the transformer, starting with the 1st and 4th, then 8th, *etc.* The embeddings for each mask location,  $j$ , and each embedding depth,  $l$ , are independently z-scored by subtracting the mean and dividing by the standard deviation over the embedding dimension,  $D$ ;  $t_{l,j} := \text{zscore}(\bar{z}_{l,j})$ . The targets for a given location  $j$  are concatenated to make a single target vector of length  $|L| \times D$  for each of the  $M$  mask patches.

*Table 1:* Results for masked self-supervised learning with Bootleg and baselines. We show the top-1 accuracy (%) for image classification on IN-1k and iNat21 using a probe on the frozen encoder (Patch, CLS, X-Blk). We also show mean-IoU (%) for semantic segmentation on ADE20K and Cityscapes using a frozen encoder (kNN, Lin, Blk). We highlight the **best** and **second best** SSL method for each architecture size. Black: Directly comparable SSL methods which do not use cross-sample interactions, trained on IN-1k. Grey: SOTA SSL models trained for longer, on larger datasets, using contrastive methods. (dst): Distilled from pretrained ViT-g.

Arch	Method	Data	Ep.	IN-1k acc.			iNat21 acc.			ADE20K mIoU			Cityscapes mIoU		
				Patch	CLS	X-Blk	Patch	CLS	X-Blk	kNN	Lin	Blk	kNN	Lin	Blk
ViT-S/16	MAE	IN-1k	800	47.0	49.8	66.4	22.3	26.2	57.5	10.2	14.1	28.7	26.9	24.7	29.3
	CrossMAE	IN-1k	800	51.8	<u>50.9</u>	<u>68.8</u>	25.7	<u>26.7</u>	<u>59.8</u>	<u>10.5</u>	<u>15.2</u>	<u>31.2</u>	25.8	<u>25.7</u>	<u>30.8</u>
	data2vec 2.0	IN-1k	200	39.9	41.7	62.2	15.4	14.6	47.4	9.5	9.6	25.4	23.3	22.2	25.8
	I-JEPA	IN-1k	600	<u>52.4</u>	N/A	61.9	26.8	N/A	48.4	8.2	11.8	21.1	17.9	19.8	24.5
	Bootleg (ours)	IN-1k	600	<b>69.8</b>	<b>70.4</b>	<b>75.3</b>	<b>42.6</b>	<b>47.8</b>	<b>67.4</b>	<b>23.5</b>	<b>26.6</b>	<b>33.9</b>	<b>29.4</b>	<b>32.1</b>	<b>35.1</b>
ViT-S/14	DINOv2 (dst)	LVD	–	77.9	<b>80.6</b>	81.5	64.2	<b>74.0</b>	78.9	34.0	39.7	42.7	39.0	46.4	47.1
ViT-B/16	MAE	IN-1k	1600	66.1	<u>67.2</u>	<u>76.0</u>	37.4	<u>43.3</u>	<u>70.7</u>	17.6	<u>24.7</u>	35.8	<u>28.0</u>	30.5	34.9
	CrossMAE	IN-1k	800	65.5	64.8	75.6	38.3	41.7	70.2	14.9	24.1	<u>36.9</u>	27.4	<u>31.2</u>	<u>36.2</u>
	data2vec 2.0	IN-1k	200	62.2	61.0	73.7	29.7	31.3	61.3	<u>17.6</u>	22.5	34.7	26.6	27.8	32.5
	I-JEPA	IN-1k	600	<u>67.0</u>	N/A	72.4	<u>41.4</u>	N/A	63.0	13.1	19.3	28.8	20.3	24.3	29.8
	Bootleg (ours)	IN-1k	600	<b>75.5</b>	<b>76.7</b>	<b>79.2</b>	<b>50.9</b>	<b>58.3</b>	<b>74.2</b>	<b>25.1</b>	<b>30.9</b>	<b>38.8</b>	<b>30.4</b>	<b>35.9</b>	<b>39.7</b>
ViT-B/14	Franca	IN-22k	(90)	<u>78.7</u>	<u>81.7</u>	<u>83.0</u>	<u>63.2</u>	<u>73.6</u>	<u>81.0</u>	<u>30.4</u>	<u>38.0</u>	<u>43.1</u>	<u>38.3</u>	<u>46.1</u>	<u>49.8</u>
	DINOv2 (dst)	LVD	–	82.2	83.7	84.2	71.4	<b>80.4</b>	<b>84.3</b>	36.0	42.8	45.8	41.4	49.6	51.1
ViT-L/16	MAE	IN-1k	1600	<u>73.0</u>	<u>75.5</u>	79.5	<u>43.9</u>	<u>51.8</u>	<u>76.3</u>	20.0	28.8	40.9	27.2	34.7	38.3
	CrossMAE	IN-1k	800	71.5	71.8	78.7	43.2	50.1	75.1	18.2	28.8	39.8	28.6	<u>36.7</u>	39.5
	data2vec 2.0	IN-1k	200	70.5	72.7	<u>80.0</u>	38.6	41.5	72.7	<u>23.4</u>	<u>30.0</u>	<b>43.0</b>	<u>28.7</u>	35.5	<b>44.3</b>
	I-JEPA	IN-1k	600	68.4	N/A	72.3	41.1	N/A	61.3	15.6	21.8	28.6	18.4	25.5	30.4
	Bootleg (ours)	IN-1k	600	<b>77.5</b>	<b>79.1</b>	<b>80.6</b>	<b>53.2</b>	<b>61.2</b>	<b>77.1</b>	<b>27.2</b>	<b>34.7</b>	<u>41.2</u>	<b>29.1</b>	<b>39.1</b>	<u>42.8</u>
ViT-L/14	CAPI	IN-1k	6394	77.6	N/A	83.2	47.6	N/A	80.7	28.6	38.9	46.1	32.9	43.7	48.1
	Franca	LAION	(3.2)	<u>82.5</u>	<u>83.4</u>	<u>84.4</u>	<u>71.5</u>	<u>77.0</u>	<u>86.2</u>	<u>33.6</u>	<u>41.7</u>	<u>46.4</u>	<u>38.5</u>	<u>48.1</u>	<u>50.6</u>
	DINOv2 (dst)	LVD	–	84.1	85.4	85.9	76.3	83.2	87.3	34.6	43.4	47.3	42.4	50.9	52.5

**Student-Encoder.** The student-encoder starts by embedding all unmasked patches into tokens. Our encoder has a further five global tokens: one class (CLS) token and four register tokens (Reg) (Darcet et al., 2024); these are concatenated to the sequence after patch tokenization. From the output of the encoder,  $z_B$ , the patch tokens and CLS token are passed to the predictor while the register tokens are discarded.

**Predictor.** For each of the four masked regions, we take the CLS and patch embeddings from the encoder and append  $|M|/4$  mask tokens. A frozen sin-cos position embedding vector is added to all tokens. The four mask regions are processed in parallel by the predictor, with self-attention allowing interaction between the tokens within a mask, but with no interaction between tokens in different mask regions. Additionally, we prepend 4 predictor-register tokens—these serve a similar “global processing” role as the register tokens in the encoder, but have their own learnable embeddings. We use a single predictor module to predict the concatenated target vector. The size of the predictor (width and depth) is unchanged from MAE—only the final linear layer is wider to project to the increased number of target elements.

## 5 Experiments

To verify the utility of the Bootleg training procedures, we perform experiments with self-supervised training on ImageNet-1k (IN-1k) (Russakovsky et al., 2015). We pretrain all ViT models on  $224 \times 224$  images with a patch size of  $16 \times 16$ . Full implementation details and hyperparameters are described in Appx. B.

For baseline comparisons, we use officially released model checkpoints where possible. For I-JEPA, no ViT-S, -B, or -L checkpoints were publicly available; we trained these using our fork of the I-JEPA codebase. For MAE (He et al., 2022) and data2vec 2.0 (Baevski et al., 2022), no ViT-S checkpoints were publicly available; we trained these using our implementation of their respective methodologies.

## 5.1 Image classification

After SSL pretraining of the ViT model with Bootleg, we evaluate the model’s performance at supervised classification of IN-1k and iNaturalist-2021 (iNat21) images. iNaturalist (Van Horn et al., 2018) is a long-tailed, fine-grained classification task with domain shift from IN-1k.

**Method.** We investigate the alignment of the unmodified embeddings from the pretrained encoder with the image classification task. This is done with a probe of the frozen encoder, which we conduct in three ways. Firstly, we consider the linear probe of the average patch embeddings (column “Patch” in tables). For this, we discard the CLS token and register tokens, take the average of the patch embeddings, apply batch norm, and add a single learnable linear layer to predict the class labels. Secondly, we consider the performance of a linear probe of the CLS token embedding (column “CLS” in tables). We take the CLS token embeddings, apply batch norm, and train a single learnable linear layer. Thirdly, we consider the performance of a non-linear attentive probe (column “X-Blk” in tables). This was performed following the implementation in V-JEPA (Bardes et al., 2024; Assran et al., 2025): we keep the patch, CLS, and any register embeddings produced by the model; these are passed to a cross-attention block with a single learnable query vector, and an MLP sub-block, followed by a linear head. We use the same width and number of attention heads as in the pretrained ViT. All probes were trained with cross-entropy for 20 epochs, with random crop, horizontal flip, and colour jitter augmentations only, and a simultaneous hyperparameter sweep of 25 learning rate and weight decay configurations. For full implementation details, see Appx. E.1.1.

**Results.** Our results, shown in Table 1, demonstrate the effectiveness of Bootleg for image classification. Across all model sizes, ViTs pretrained with Bootleg outperform the within-category competitors. This demonstrates the effectiveness of the pretraining methodology at learning to represent high-level image features. The largest margins (> 10%) were seen at the smallest model sizes. With full fine-tuning (see Appx. F.2) the models are better able to align their final embeddings with the classification task so there is less variation in performance among models; frozen evaluations are more indicative of the quality of the learnt representations.

## 5.2 Semantic segmentation

**Method.** To check the performance of ViTs pretrained with Bootleg on a standard dense-prediction task, we run experiments on the ADE20K (Zhou et al., 2017) and Cityscapes (Cordts et al., 2016) semantic segmentation benchmarks.

First, we probe using the kNN methodology from CAPI (Darcet et al., 2025). For this probe, images from the training partition are encoded without augmentations. The embeddings and pixel-wise segmentation labels for each patch token form the kNN training set; inference is performed by finding the  $k$  nearest neighbours for each patch in the image and then using a majority vote across them for the class of each pixel. We sweep 4 neighbourhood sizes.

Next we probe using a Segmenter (Strudel et al., 2021) head trained atop a frozen backbone. We consider two heads, trained separately: (Lin) a linear projector from the patch embeddings to the Segmenter, or (Blk) with one randomly initialized transformer block before the projector. Our training strategy is based on the BEiT evaluation methodology (Bao et al., 2022); we train for 128 epochs with a batch size of 64, and augment the data with random resized cropping, horizontal flips, cut-out, and colour jitter. We sweep 4 LRs for each head type. For full implementation details, see Appx. E.2.

**Results.** As shown in Table 1, Bootleg performs competitively at semantic segmentation. The frozen probes show Bootleg is much better able to perform pixel-level segmentation than its self-distillation competitor, I-JEPA, demonstrating that distillation of features along the visual pathway facilitates the model’s ability to perform at a range of levels of granularity.

## 5.3 Additional evaluations

We evaluated the pretrained models with fine-tuning on IN-1k and ADE20K, as described in Appx. F.2. Bootleg performed best for full fine-tuning on IN-1k with 100% or 1% (low-shot) of the training data, although the margins are smaller than for the probing evaluation because the models are trained further. For LoRA fine-tuning on IN-1k and full finetuning on ADE20K, Bootleg performs best for ViT-S and B, and data2vec best for ViT-L.

We evaluated the pretrained models on the Visual Task Adaptation Benchmark (VTAB) (Zhai et al., 2019), as described in Appx. F.3. Our results show Bootleg models excel at representing naturalistic images (those corresponding to the IN-1k pretraining domain) and specialized imagery (e.g. satellite and medical images), but

are less performant on synthetic images (e.g. Clevr, dSprites).

## 6 Ablations

We ablate key elements of our method, compare related extensions of other methods, and closely study the differences with I-JEPA.

### 6.1 Choice of target layers

The core mechanism of Bootleg is the self-distillation of hidden layers—which poses the question of which hidden layers to distil. We explore the performance of ViT-S, -B, -L with different hidden targets for self-distillation during pretraining. In addition to predicting the output of various hidden blocks,  $z_l$ , we explore the performance when predicting the mid-block representations,  $z_l^{\text{mid}}$ , and the residual terms  $r_l^{\text{Attn}}$  and  $r_l^{\text{MLP}}$  (tabulated in Appx. G.2.1). For ViT-S, we find two peaks in performance: one when using 3–4 equispaced block outputs as targets, and another when targeting multiple layers within every block. However, targeting the residual layers was only sometimes beneficial, and only seen for ViT-S. Overall, targeting the output of every fourth block in the teacher is a rule-of-thumb which gives consistently strong performance, and often the best performance of the configurations tried.

In addition to investigating how many hidden layers to target and their types, we consider where the targets should be taken from. As shown in Table 2, we found using four spaced-out targets outperforms using consecutive targets from the start, middle, or final blocks of the teacher. Data2vec uses an average of the final 10 layers as its target, implicitly assuming the training signal across multiple hidden layers can be linearly integrated together. We, on the other hand, use a concatenation of the latent embeddings from multiple blocks as the distillation target, treating latents as distinct representations of intermediate abstraction. Using multiple layers of abstraction as distillation training targets improves performance over distilling a single target (Table 2).

Table 2: Target construction strategy. We compare four spaced-out targets (ours) to consecutive targets from the early, middle, or final layers of the network. We also consider two options of how to merge targets: either standardize and concatenate (ours) or standardize, average, and re-standardize (data2vec-style). Spaced-out, concatenated, targets yield the best training targets. Experiments trained for 300 ep. on IN-1k (based on our final training recipe; see Appx. B) and evaluated with frozen probe.

Targets	Merge op.	IN-1k acc.			ADE20K mIoU		
		Patch	CLS	X-Blk	kNN	Lin	Blk
Pixel targets (MAE-style)	N/A	52.9	51.0	66.7	13.6	17.7	27.5
Blocks 1–4 (early only)	Concat	58.0	57.1	69.5	16.5	21.0	30.1
Blocks 5–8 (mid only)	Concat	61.6	61.7	72.2	18.6	23.0	33.0
Blocks 3–12 (last 10)	Concat	<u>64.6</u>	<u>66.0</u>	<u>73.4</u>	<u>20.9</u>	<u>24.5</u>	<u>33.4</u>
Blocks 9–12 (late only)	Concat	60.2	60.8	69.7	16.0	19.7	29.3
Blocks {1, 4, 8, 12} (spaced)	Concat	<b>67.8</b>	<b>68.9</b>	<b>74.4</b>	<b>22.1</b>	<b>26.6</b>	<b>34.2</b>
Blocks 3–12 (last 10; d2v-style)	Average	44.1	37.9	59.9	8.8	12.8	24.2
Blocks {1, 4, 8, 12} (spaced)	Average	57.2	54.6	69.8	15.6	19.8	30.5

### 6.2 Bootleg editions of other masking methods

We explore the effect of adding our main conceptual contribution—self-distillation of hidden layers—to other masked image modelling methods with minimal other changes (Table 3). We train a ViT-S for 300 epochs on IN-1k using either the MAE, CrossMAE, data2vec 2.0, or I-JEPA framework, then evaluate with frozen probes on IN-1k, as described in Sec. 5.1.

**Adding EMA.** To facilitate self-distillation, we need to add an EMA teacher to MAE and CrossMAE; we first evaluate the performance of the EMA encoder without using it for distillation. Its performance is negligibly different from that of the encoder without EMA.

**Masking.** As we show in Sec. 3.2, the masking strategy of MAE is a limiting factor for the adoption of self-distillation of targets deeper than Block 2. We thus change its masking strategy to our implementation of I-JEPA masking, which improved performance. For MAE and data2vec, we also apply the predictor once per mask region, allowing self-attention interactions within the tokens of each region. For CrossMAE, the use of cross- instead of

self-attention means there is no interaction between the mask tokens, and so this is not a consideration; we use the concatenation of the mask tokens from all four regions for efficiency<sup>1</sup>.

**ViT predictor.** Data2vec 2.0 uses a light-weight CNN predictor module (much smaller than the ViT predictors used by MAE and I-JEPA), which lacks the capacity to handle predicting multiple target vectors. We hence changed the data2vec 2.0 predictor to our ViT architecture, yielding a significant performance gain.

**Hidden-self-distillation.** With these changes in place, we next change the target from the image pixels (MAE and CrossMAE), final layer (I-JEPA), and average over multiple layers (data2vec 2.0), to our target: a concatenation of hidden latent vectors. This greatly increases the performances for MAE and CrossMAE (+10% Patch and CLS probes, +6% to X-Blk probes) and I-JEPA (+6%). For data2vec 2.0, using the concatenation of hidden layers instead of their average improves performance (+2%), but changing the targets from the final 10 layers to every 4th layer does not (−1%). These findings indicate masked image modelling can in general benefit from using our hidden-self-distillation, provided the masking strategy supports it.

Table 3: Effect of combining key Bootleg components with existing pretraining methods. Experiments conducted with ViT-S, 300 ep., and evaluated with frozen probe on IN-1k (top-1 acc, %) and ADE20K (mIoU, %). Modifications are cumulative. See Sec. 6.2 for details.

Base	Modification	IN-1k acc.			ADE20K mIoU	
		Patch	CLS	X-Blk	kNN	Lin
MAE	Unmodified	44.7	47.0	65.1	9.3	13.1
	+EMA	44.8 +0.1	46.9 −0.1	65.1 −0.0	9.1 −0.2	13.1 −0.0
	+our masking	51.2 +6.5	50.7 +3.8	66.0 +0.9	12.2 +3.1	16.6 +3.5
	+change targets	62.4 +11.2	62.9 +12.2	72.1 +6.1	19.5 +7.3	24.1 +7.4
CrossMAE	Unmodified	45.7	44.4	65.2	8.5	12.7
	+EMA	45.7 +0.0	44.3 −0.1	65.3 +0.1	8.6 +0.1	12.7 +0.0
	+our masking	51.5 +5.7	52.5 +8.2	66.6 +1.3	10.3 +1.7	15.8 +3.1
	+change targets	60.8 +9.4	61.6 +9.1	71.8 +5.3	14.6 +4.4	21.4 +5.5
data2vec 2.0	300ep, 4 mask reps	40.9	40.3	61.4	8.8	−
	+our masking	44.4 +3.5	49.2 +8.8	64.3 +2.9	9.8 +1.0	10.5
	+our ViT predictor	58.8 +14.4	53.7 +4.6	70.7 +6.4	15.4 +5.5	20.5 +10.1
	+concat targets	60.9 +2.1	52.5 −1.2	72.2 +1.5	18.3 +2.9	22.9 +2.4
	+change targets	60.2 −0.7	50.0 −2.5	71.7 −0.6	17.6 −0.7	22.1 −0.9
I-JEPA	Unmodified	53.4	N/A	62.3	10.5	13.5
	+change targets	59.5 +6.1	N/A	69.3 +7.0	15.1 +4.6	19.3 +5.7

### 6.3 Interpolating between I-JEPA and Bootleg

We carefully identify and evaluate the differences between Bootleg and the closest existing masked image modelling method: I-JEPA. As shown in Table 4, we find changing the targets to be the outputs of multiple blocks is the largest single improvement made to the I-JEPA training configuration, followed by improving the implementation of the masking strategy and the addition of a CLS token. However, our final Bootleg training recipe is more heavily impacted by ablating features such as the larger predictor (which facilitates processing additional targets) than ablating the number of targets.

### 6.4 Changing masking strategy

We ablated our masking strategy, using methods from recent papers. The results are shown in Table 5.

When training with uniform random masks as per MAE, training became unstable after 160 epochs and the model collapsed. Using “green” structured noise from ColorMAE Hinojosa et al. (2025) or inverse-blocks as per data2vec Baevski et al. (2023), training was unstable and performance suffered as a result, but not as badly as when using random noise. In contrast to this, cyclic block masking, used by CAPI and Franca (Darcet et al., 2025; Venkataramanan et al., 2025), yielded stable training and even out-performed the I-JEPA implementation of multi-block masking.

<sup>1</sup>Note that the overlap of mask regions means there are redundant mask tokens for the same patch location for the CrossMAE predictor; these serve only to increase the loss weighting on resampled mask locations, and for consistency we did not deduplicate these.

Table 4: Ablation of the differences between I-JEPA and Bootleg. Each row isolates a single change to the training configuration. We show the performance of a model trained with a config equal to I-JEPA plus one change from Bootleg (“Only with”), and with a config equivalent to changing everything from the I-JEPA to Bootleg config except for one component (“Only without”). Next to each of these is the change in accuracy observed when adding that first component to I-JEPA’s config, and when adding it as the final component to reach Bootleg. Changes between rows are not cumulatively stacked on top of each other. Experiments performed with ViT-S, 300 ep.

Ablation	IN-1k acc., X-Blk probe				ADE mIoU, Lin probe				Avg $\Delta$
	Only with		Only without		Only with		Only without		
I-JEPA (= with none)	62.3				13.5				
Data transforms: +hflip, $\uparrow$ min crop size	63.2	+0.8	74.2	+0.2	13.3	-0.2	25.8	+0.8	+0.4
Add CLS token	65.9	+3.5	74.1	+0.3	17.4	+3.9	25.6	+1.0	+2.2
Add 4/4 reg tokens to encoder/predictor	64.7	+2.4	73.9	+0.5	15.5	+1.9	25.6	+1.0	+1.4
Predictor size: $\uparrow$ depth, $\uparrow$ heads	64.1	+1.8	72.5	+1.9	13.9	+0.3	23.6	+3.0	+1.8
Masking: implementation improvements	68.2	+5.9	72.6	+1.8	18.0	+4.5	24.5	+2.2	+3.6
Targets: $T = \{12\} \rightarrow \{1, 4, 8, 12\}$	69.3	+7.0	73.9	+0.4	19.3	+5.7	25.2	+1.4	+3.6
Loss: Smooth L1 $\rightarrow$ L2	65.1	+2.7	74.5	-0.1	14.9	+1.3	25.5	+1.1	+1.3
Hyperparams: $\uparrow$ LR, $\uparrow$ WU, $\downarrow$ WD	63.7	+1.3	73.1	+1.2	13.0	-0.5	24.1	+2.5	+1.2
Bootleg (= with all)	74.4				26.6				

Table 5: Changing masking strategy. Experiments trained for 300 ep. on IN-1k whilst using different masking strategies. Evaluated with frozen probe on IN-1k and ADE20K.

Masking strategy	Seen (%)	Target (%)	IN-1k acc.			ADE20K mIoU		
			Patch	CLS	X-Blk	kNN	Lin	Blk
Random (MAE-style)	25.0	75.0	2.6	2.5	10.9	2.3	1.4	4.3
Green noise (ColorMAE-style)	25.0	75.0	36.0	32.0	58.3	7.6	10.5	23.5
Inverse block (data2vec-style; 1 rep.)	20.0	80.0	58.0	53.6	69.5	16.3	21.5	30.2
Inverse block (data2vec-style; 4 rep.)	20.0	80.0	59.2	53.1	70.1	16.9	21.1	31.8
Cyclic block (Franca/CAP1)	25.0 (20–30)	75.0 (70–80)	67.0	65.8	73.7	20.8	25.1	32.2
Cyclic block (Franca/CAP1)	30.0 (25–35)	70.0 (65–75)	<b>68.0</b>	<u>67.4</u>	<u>74.0</u>	<u>21.4</u>	<u>25.8</u>	<u>32.4</u>
Multi-block (I-JEPA)	24.3 ( 9–37)	44.5 (24–64)	65.3	66.5	72.6	20.6	24.5	31.7
Multi-block (ours)	29.2 (13–43)	47.5 (26–71)	<u>67.8</u>	<b>68.9</b>	<b>74.4</b>	<b>22.1</b>	<b>26.6</b>	<b>34.2</b>

The key difference between these masking strategies is the size of the contiguous blocks which are masked out—larger mask sizes yielded better performance. We hypothesize this is because neighbouring patch tokens have highly correlated activations, especially deeper in the visual hierarchy. Hence it is important that the majority of target patches are not adjacent to a seen patch, otherwise the model learns to use the short-cut. This observation is comparable to that found in contrastive learning, where heavy colour augmentations need to be applied on the views to prevent the model from using correlations in the RGB histogram as a short-cut to solve the task (Chen et al., 2020a).

## 7 Related Work

We group SSL algorithms into two categories: single-view and multi-view methods. Single-view methods, such as MAE, I-JEPA, and our Bootleg, have two key advantages: (1) they do not require hand-crafted data augmentation strategies or rules to generate pairs of “positive” views to promote embedding similarity, and (2) they are independent of batch size since they do not require (explicit or implicit) “negatives” to promote embedding dissimilarity and avoid representational collapse. By not requiring large batches, single-view methods are more accessible and can be pretrained on a single consumer GPU. By not requiring data augmentation strategies, single-view methods can be easily adapted to other domains and input shapes (e.g., time series, 3D point clouds, etc.). We thus restrict our experimental comparisons of Bootleg to comparable single-view methods.

**Single-view methods do *not* require augmentations or large batches.** The first masked modelling methods for imagery encode *mask tokens* alongside patch tokens, following BERT in natural language (Devlin et al., 2019). They are pretrained to predict the masked-out pixels (Xie et al., 2022; Dosovitskiy et al., 2021), discrete patch tokens (Bao et al., 2022; Dong et al., 2023), or features (Zhou et al., 2022; Wei et al., 2022) with a small decoder. MAE

(He et al., 2022) introduced encoding visible tokens *only* (no mask tokens) and a larger decoder, which reduces computation and improves representations; this token-dropping method has been widely leveraged since, e.g., by data2vec 2.0 (Baevski et al., 2023), I-JEPA (Assran et al., 2023), and CrossMAE (Fu et al., 2025). CrossMAE replaces MAE’s self-attention-based decoder with a cross-attention-based decoder for reduced pretraining computation with similar downstream accuracy. Our Bootleg follows MAE/I-JEPA’s asymmetric encoder-decoder design for efficient pretraining.

**Multi-view methods require augmentations and large batches.** Canonical contrastive learning algorithms (Chen et al., 2020b, 2021, 2020a) promote embedding similarity (for positives) and dissimilarity (for negatives) via InfoNCE-style losses (van den Oord et al., 2018). And C-JEPA (Mo & Tong, 2024) adds a contrastive-loss term to I-JEPA. Other methods such as iBOT (Zhou et al., 2022) and CAPI (Darcet et al., 2025) merge contrastive objectives with masked imagery. These contrastive algorithms, such as Sinkhorn-Knopp (Caron et al., 2020), require batches that contain several thousand samples, and multi-GPU training to meet their memory requirements. Methods such as Barlow Twins (Zbontar et al., 2021), VICReg (Bardes et al., 2022), and MMCR (Yerxa et al., 2023), use several hundred samples per batch, at minimum, and promote similarity between positives generated via data augmentation. These new methods spread-out the embedding space over the batch, for example by encouraging the standard deviation of each embedding dimension—calculated per batch, and is thus batch-size dependent—to be above a threshold. Similarly, Bootstrap Your Own Latent (BYOL, (Grill et al., 2020)) was an earlier method that also requires implicit negatives to avoid collapse. It partially inspires our Bootleg name. State-of-the-art image SSL methods such as DINOv2 (Oquab et al., 2024) and Franca (Venkataramanan et al., 2025) have many self-supervised objectives, some of which also require multiple views and large batches (e.g. 16,384). Our Bootleg does *not* require data augmentation, thus is more general and less domain-specific, and can be pretrained with a single GPU, thus is more accessible.

## 8 Discussion

We have presented Bootleg, a novel method for self-supervised representation learning of images. Our method uses hidden-self-distillation: the student must learn to predict latent representations from hidden layers within the teacher.

**Strengths.** We have demonstrated hidden-self-distillation is a powerful pretraining method for representation learning and lends itself to creating embeddings well aligned with image classification, without needing labels during training. It does not use any within-batch interactions, meaning it can be readily deployed across a range of hardware even with small batch sizes. Furthermore, training does not rely on any domain-specific augmentations, so could be deployed in other domains with minimal modification.

**Limitations.** Like other self-distillation techniques, our method makes use of a teacher-encoder. This has a non-trivial computational overhead (around 12% of total training time), since the teacher sees all of the stimulus. Although we use more targets than I-JEPA, generating these does not require any additional passes through the teacher-encoder, as all targets for Bootleg can be collected in one pass. As Bootleg does use more targets, there is additional processing overhead for them (indexing mask locations and z-scoring embeddings), and for computation of the loss. However, when using every 4th block as a target, these costs only amount to 2% training time, and is mitigated by only computing the gradient of the loss rather than the loss itself on most steps. Our remaining limitation is the requirement of a sufficiently sophisticated masking strategy to reduce correlations between seen and neighbouring target tokens. We leave open to future work the challenge of choosing an appropriate masking strategy for a given training dataset.

## Acknowledgements

Resources used in preparing this research were provided, in part, by the Province of Ontario, the Government of Canada through CIFAR, and [companies sponsoring](#) the Vector Institute.

Thanks to Patrik Reizinger for insightful discussions.

## Author contributions

Scott C. Lowe: conceptualization, methodology, investigation, writing (original draft), visualization. Anthony Fuller: methodology, writing (original draft). Sageev Oore: writing (review & editing). Evan Shelhamer: writing (review & editing). Graham W. Taylor: writing (review & editing), funding acquisition.

## References

- Mahmoud Assran, Quentin Duval, Ishan Misra, Piotr Bojanowski, Pascal Vincent, Michael Rabbat, Yann LeCun, and Nicolas Ballas. Self-supervised learning from images with a joint-embedding predictive architecture. In *Proceedings of the IEEE/CVF Conference on Computer Vision and Pattern Recognition (CVPR)*, pp. 15619–15629, 2023. doi:10.1109/CVPR52729.2023.01499. 1, 3, 4, 10, 17, 18, 26, 37
- Mahmoud Assran, Adrien Bardes, David Fan, Quentin Garrido, Russell Howes, Mojtaba Komeili, Matthew Muckley, Ammar Rizvi, Claire Roberts, Koustuv Sinha, Artem Zhohus, Sergio Arnaud, Abha Gejji, Ada Martin, Francois Robert Hogan, Daniel Dugas, Piotr Bojanowski, Vasil Khalidov, Patrick Labatut, Francisco Massa, Marc Szafraniec, Kapil Krishnakumar, Yong Li, Xiaodong Ma, Sarath Chandar, Franziska Meier, Yann LeCun, Michael Rabbat, and Nicolas Ballas. V-JEPA 2: Self-supervised video models enable understanding, prediction and planning. *arXiv preprint arXiv:2506.09985*, 2025. doi:10.48550/arxiv.2506.09985. 1, 6, 17, 18, 25
- Roman Bachmann, David Mizrahi, Andrei Atanov, and Amir Zamir. MultiMAE: Multi-modal multi-task masked autoencoders. In Shai Avidan, Gabriel Brostow, Moustapha Cissé, Giovanni Maria Farinella, and Tal Hassner (eds.), *Computer Vision – ECCV 2022*, pp. 348–367, Cham, 2022. Springer Nature Switzerland. ISBN 978-3-031-19836-6. doi:10.1007/978-3-031-19836-6\_20. URL [https://www.ecva.net/papers/eccv\\_2022/papers\\_ECCV/html/7102\\_ECCV\\_2022\\_paper.php](https://www.ecva.net/papers/eccv_2022/papers_ECCV/html/7102_ECCV_2022_paper.php). 1
- Alexei Baeviski, Wei-Ning Hsu, Qiantong Xu, Arun Babu, Jiatao Gu, and Michael Auli. data2vec: A general framework for self-supervised learning in speech, vision and language. In Kamalika Chaudhuri, Stefanie Jegelka, Le Song, Csaba Szepesvari, Gang Niu, and Sivan Sabato (eds.), *Proceedings of the 39th International Conference on Machine Learning*, volume 162 of *Proceedings of Machine Learning Research*, pp. 1298–1312. PMLR, 17–23 Jul 2022. URL <https://proceedings.mlr.press/v162/baeviski22a.html>. 2, 5
- Alexei Baeviski, Arun Babu, Wei-Ning Hsu, and Michael Auli. Efficient self-supervised learning with contextualized target representations for vision, speech and language. In Andreas Krause, Emma Brunskill, Kyunghyun Cho, Barbara Engelhardt, Sivan Sabato, and Jonathan Scarlett (eds.), *Proceedings of the 40th International Conference on Machine Learning*, volume 202 of *Proceedings of Machine Learning Research*, pp. 1416–1429. PMLR, 23–29 Jul 2023. URL <https://proceedings.mlr.press/v202/baeviski23a.html>. 2, 8, 10
- Hangbo Bao, Li Dong, Songhao Piao, and Furu Wei. BEiT: BERT pre-training of image transformers. In *International Conference on Learning Representations*, 2022. URL <https://openreview.net/forum?id=p-BhZSz59o4>. 6, 9, 27
- Adrien Bardes, Jean Ponce, and Yann LeCun. VICReg: Variance-invariance-covariance regularization for self-supervised learning. In *International Conference on Learning Representations*, 2022. URL <https://openreview.net/forum?id=xm6YD62D1Ub>. 10
- Adrien Bardes, Quentin Garrido, Jean Ponce, Xinlei Chen, Michael Rabbat, Yann LeCun, Mido Assran, and Nicolas Ballas. Revisiting feature prediction for learning visual representations from video. *Transactions on Machine Learning Research*, 2024. ISSN 2835-8856. doi:10.48550/arxiv.2404.08471. Featured Certification. 1, 6, 17, 25
- David Bau, Bolei Zhou, Aditya Khosla, Aude Oliva, and Antonio Torralba. Network dissection: Quantifying interpretability of deep visual representations. In *Proceedings of the IEEE/CVF Conference on Computer Vision and Pattern Recognition (CVPR)*, pp. 3319–3327, 2017. doi:10.1109/CVPR.2017.354. 3
- Daniel Bolya, Po-Yao Huang, Peize Sun, Jang Hyun Cho, Andrea Madotto, Chen Wei, Tengyu Ma, Jiale Zhi, Jathushan Rajasegaran, Hanoona Abdul Rasheed, Junke Wang, Marco Monteiro, Hu Xu, Shiyu Dong, Nikhila Ravi, Shang-Wen Li, Piotr Dollar, and Christoph Feichtenhofer. Perception encoder: The best visual embeddings are not at the output of the network. In *The Thirty-ninth Annual Conference on Neural Information Processing Systems*, 2025. URL <https://openreview.net/forum?id=INqB0mwIpG>. 3
- Mathilde Caron, Ishan Misra, Julien Mairal, Priya Goyal, Piotr Bojanowski, and Armand Joulin. Unsupervised learning of visual features by contrasting cluster assignments. In H. Larochelle, M. Ranzato, R. Hadsell, M.F. Balcan, and H. Lin (eds.), *Advances in Neural Information Processing Systems*, volume 33, pp. 9912–9924. Curran Associates, Inc., 2020. URL [https://proceedings.neurips.cc/paper\\_files/paper/2020/file/70feb62b69f16e0238f741fab228fec2-Paper.pdf](https://proceedings.neurips.cc/paper_files/paper/2020/file/70feb62b69f16e0238f741fab228fec2-Paper.pdf). 10
- Anthony Chen, Kevin Zhang, Renrui Zhang, Zihan Wang, Yuheng Lu, Yandong Guo, and Shanghang Zhang. PiMAE: Point cloud and image interactive masked autoencoders for 3d object detection. In *Proceedings of the IEEE/CVF Conference on Computer Vision and Pattern Recognition (CVPR)*, pp. 5291–5301, 2023. doi:10.1109/CVPR52729.2023.00512. 1
- Delong Chen, Mustafa Shukor, Theo Moutakanni, Willy Chung, Jade Yu, Tejaswi Kasarla, Yejin Bang, Allen Bolourchi, Yann LeCun, and Pascale Fung. VL-JEPA: Joint embedding predictive architecture for vision-language. *arXiv preprint arXiv:2512.10942*, 2025. doi:10.48550/arxiv.2512.10942. 1
- Ting Chen, Simon Kornblith, Mohammad Norouzi, and Geoffrey Hinton. A simple framework for contrastive learning of visual representations. In Hal Daumé III and Aarti Singh (eds.), *Proceedings of the 37th International Conference on Machine Learning*, volume 119 of *Proceedings of Machine Learning Research*, pp. 1597–1607. PMLR, 13–18 Jul 2020a. URL <https://proceedings.mlr.press/v119/chen20j.html>. 9, 10, 26

- Xinlei Chen and Kaiming He. Exploring simple siamese representation learning. In *Proceedings of the IEEE/CVF Conference on Computer Vision and Pattern Recognition (CVPR)*, pp. 15745–15753, 2021. doi:[10.1109/CVPR46437.2021.01549](https://doi.org/10.1109/CVPR46437.2021.01549). 37
- Xinlei Chen, Haoqi Fan, Ross Girshick, and Kaiming He. Improved baselines with momentum contrastive learning. *arXiv preprint arXiv:2003.04297*, 2020b. doi:[10.48550/arxiv.2003.04297](https://doi.org/10.48550/arxiv.2003.04297). 10
- Xinlei Chen, Saining Xie, and Kaiming He. An empirical study of training self-supervised vision transformers. In *Proceedings of the IEEE/CVF International Conference on Computer Vision (ICCV)*, pp. 9620–9629, 2021. doi:[10.1109/ICCV48922.2021.00950](https://doi.org/10.1109/ICCV48922.2021.00950). 10
- Andy Clark. Whatever next? Predictive brains, situated agents, and the future of cognitive science. *Behav Brain Sci*, 36(3): 181–204, May 2013. doi:[10.1017/s0140525x12000477](https://doi.org/10.1017/s0140525x12000477). 3
- Yezhen Cong, Samar Khanna, Chenlin Meng, Patrick Liu, Erik Rozi, Yutong He, Marshall Burke, David Lobell, and Stefano Ermon. SatMAE: Pre-training transformers for temporal and multi-spectral satellite imagery. In S. Koyejo, S. Mohamed, A. Agarwal, D. Belgrave, K. Cho, and A. Oh (eds.), *Advances in Neural Information Processing Systems*, volume 35, pp. 197–211. Curran Associates, Inc., 2022. URL [https://proceedings.neurips.cc/paper\\_files/paper/2022/file/01c561df365429f33fcd7a7faa44c985-Paper-Conference.pdf](https://proceedings.neurips.cc/paper_files/paper/2022/file/01c561df365429f33fcd7a7faa44c985-Paper-Conference.pdf). 1
- Marius Cordts, Mohamed Omran, Sebastian Ramos, Timo Rehfeld, Markus Enzweiler, Rodrigo Benenson, Uwe Franke, Stefan Roth, and Bernt Schiele. The cityscapes dataset for semantic urban scene understanding. In *Proceedings of the IEEE Conference on Computer Vision and Pattern Recognition (CVPR)*, pp. 3213–3223, June 2016. 6
- Timothée Darcet, Maxime Oquab, Julien Mairal, and Piotr Bojanowski. Vision transformers need registers. In *The Twelfth International Conference on Learning Representations*, 2024. URL <https://openreview.net/forum?id=2dn03LLiJ1>. 2, 5, 17
- Timothée Darcet, Federico Baldassarre, Maxime Oquab, Julien Mairal, and Piotr Bojanowski. Cluster and predict latents patches for improved masked image modeling. *Transactions on Machine Learning Research*, 2025. ISSN 2835-8856. URL <https://openreview.net/forum?id=Ycmz7qJxUQ>. 6, 8, 10, 26
- Jacob Devlin, Ming-Wei Chang, Kenton Lee, and Kristina Toutanova. BERT: Pre-training of deep bidirectional transformers for language understanding. In Jill Burstein, Christy Doran, and Thamar Solorio (eds.), *Proceedings of the 2019 Conference of the North American Chapter of the Association for Computational Linguistics: Human Language Technologies, Volume 1 (Long and Short Papers)*, pp. 4171–4186, Minneapolis, Minnesota, June 2019. Association for Computational Linguistics. doi:[10.18653/v1/N19-1423](https://doi.org/10.18653/v1/N19-1423). 9
- Xiaoyi Dong, Jianmin Bao, Ting Zhang, Dongdong Chen, Weiming Zhang, Lu Yuan, Dong Chen, Fang Wen, Nenghai Yu, and Baining Guo. PeCo: Perceptual codebook for BERT pre-training of vision transformers. In *Proceedings of the AAAI Conference on Artificial Intelligence*, volume 37, pp. 552–560, Jun 2023. doi:[10.1609/aaai.v37i1.25130](https://doi.org/10.1609/aaai.v37i1.25130). 9
- Zijian Dong, Ruilin Li, Yilei Wu, Thuan Tinh Nguyen, Joanna Su Xian Chong, Fang Ji, Nathanael Ren Jie Tong, Christopher Li Hsian Chen, and Juan Helen Zhou. Brain-JEPA: Brain dynamics foundation model with gradient positioning and spatiotemporal masking. In A. Globerson, L. Mackey, D. Belgrave, A. Fan, U. Paquet, J. Tomczak, and C. Zhang (eds.), *Advances in Neural Information Processing Systems*, volume 37, pp. 86048–86073. Curran Associates, Inc., 2024. doi:[10.52202/079017-2732](https://doi.org/10.52202/079017-2732). URL [https://proceedings.neurips.cc/paper\\_files/paper/2024/file/9c3828adf1500f5de3c56f6550dfe43c-Paper-Conference.pdf](https://proceedings.neurips.cc/paper_files/paper/2024/file/9c3828adf1500f5de3c56f6550dfe43c-Paper-Conference.pdf). 1
- Alexey Dosovitskiy, Lucas Beyer, Alexander Kolesnikov, Dirk Weissenborn, Xiaohua Zhai, Thomas Unterthiner, Mostafa Dehghani, Matthias Minderer, Georg Heigold, Sylvain Gelly, Jakob Uszkoreit, and Neil Houlsby. An image is worth 16x16 words: Transformers for image recognition at scale. In *International Conference on Learning Representations*, 2021. URL <https://openreview.net/forum?id=YicbFdNTTy>. 1, 9
- Utku Evci, Vincent Dumoulin, Hugo Larochelle, and Michael C. Mozer. Head2Toe: Utilizing intermediate representations for better transfer learning. In Kamalika Chaudhuri, Stefanie Jegelka, Le Song, Csaba Szepesvari, Gang Niu, and Sivan Sabato (eds.), *Proceedings of the 39th International Conference on Machine Learning*, volume 162 of *Proceedings of Machine Learning Research*, pp. 6009–6033. PMLR, 17–23 Jul 2022. URL <https://proceedings.mlr.press/v162/evci22a.html>. 3
- Zhengcong Fei, Mingyuan Fan, and Junshi Huang. A-JEPA: Joint-embedding predictive architecture can listen. *arXiv preprint arXiv:2311.15830*, 2024. doi:[10.48550/arxiv.2311.15830](https://doi.org/10.48550/arxiv.2311.15830). 1
- Karl Friston. A theory of cortical responses. *Philosophical Transactions of the Royal Society B: Biological Sciences*, 360(1456): 815–836, 2005. doi:[10.1098/rstb.2005.1622](https://doi.org/10.1098/rstb.2005.1622). 3
- Karl Friston and Stefan Kiebel. Predictive coding under the free-energy principle. *Philos Trans R Soc Lond B Biol Sci*, 364(1521): 1211–1221, May 2009. doi:[10.1098/rstb.2008.0300](https://doi.org/10.1098/rstb.2008.0300). 3
- Letian Fu, Long Lian, Renhao Wang, Baifeng Shi, XuDong Wang, Adam Yala, Trevor Darrell, Alexei A. Efros, and Ken Goldberg. Rethinking patch dependence for masked autoencoders. *Transactions on Machine Learning Research*, 2025. ISSN 2835-8856. URL <https://openreview.net/forum?id=JT2KMuo2BV>. 10, 18, 26, 36

- Anthony Fuller, Koreen Millard, and James R. Green. SatViT: Pretraining transformers for earth observation. *IEEE Geoscience and Remote Sensing Letters*, 19:1–5, 2022. doi:[10.1109/LGRS.2022.3201489](https://doi.org/10.1109/LGRS.2022.3201489). 1
- Jean-Bastien Grill, Florian Strub, Florent Altché, Corentin Tallec, Pierre Richemond, Elena Buchatskaya, Carl Doersch, Bernardo Avila Pires, Zhaohan Guo, Mohammad Gheshlaghi Azar, Bilal Piot, koray kavukcuoglu, Remi Munos, and Michal Valko. Bootstrap your own latent - a new approach to self-supervised learning. In H. Larochelle, M. Ranzato, R. Hadsell, M.F. Balcan, and H. Lin (eds.), *Advances in Neural Information Processing Systems*, volume 33, pp. 21271–21284. Curran Associates, Inc., 2020. URL [https://proceedings.neurips.cc/paper\\_files/paper/2020/file/f3ada80d5c4ee70142b17b8192b2958e-Paper.pdf](https://proceedings.neurips.cc/paper_files/paper/2020/file/f3ada80d5c4ee70142b17b8192b2958e-Paper.pdf). 10, 37
- Rafik Hachana and Bader Rasheed. Using a joint-embedding predictive architecture for symbolic music understanding. In *AI for Music Workshop*, 2025. URL <https://openreview.net/forum?id=lieErtGZb6>. 1
- Kaiming He, Xinlei Chen, Saining Xie, Yanghao Li, Piotr Dollár, and Ross Girshick. Masked autoencoders are scalable vision learners. In *Proceedings of the IEEE/CVF Conference on Computer Vision and Pattern Recognition (CVPR)*, pp. 15979–15988, 2022. doi:[10.1109/CVPR52688.2022.01553](https://doi.org/10.1109/CVPR52688.2022.01553). 1, 5, 10, 17, 36
- Carlos Hinojosa, Shuming Liu, and Bernard Ghanem. ColorMAE: Exploring data-independent masking strategies in masked autoencoders. In Aleš Leonardis, Elisa Ricci, Stefan Roth, Olga Russakovsky, Torsten Sattler, and Gül Varol (eds.), *Computer Vision – ECCV 2024*, pp. 432–449, Cham, 2025. Springer Nature Switzerland. ISBN 978-3-031-72661-3. doi:[10.1007/978-3-031-72661-3\\_25](https://doi.org/10.1007/978-3-031-72661-3_25). URL [https://www.ecva.net/papers/eccv\\_2024/papers\\_ECCV/html/3072\\_ECCV\\_2024\\_paper.php](https://www.ecva.net/papers/eccv_2024/papers_ECCV/html/3072_ECCV_2024_paper.php). 8
- Tomoyasu Horikawa and Yukiyasu Kamitani. Generic decoding of seen and imagined objects using hierarchical visual features. *Nature Communications*, 8(1):15037, May 2017. ISSN 2041-1723. doi:[10.1038/ncomms15037](https://doi.org/10.1038/ncomms15037). 3
- Edward J. Hu, Yelong Shen, Phillip Wallis, Zeyuan Allen-Zhu, Yanzhi Li, Shean Wang, Lu Wang, and Weizhu Chen. LoRA: Low-rank adaptation of large language models. In *International Conference on Learning Representations*, 2022. URL <https://openreview.net/forum?id=nZvKeeFYf9>. 26
- Po-Yao Huang, Hu Xu, Juncheng Li, Alexei Baevski, Michael Auli, Wojciech Galuba, Florian Metzger, and Christoph Feichtenhofer. Masked autoencoders that listen. In S. Koyejo, S. Mohamed, A. Agarwal, D. Belgrave, K. Cho, and A. Oh (eds.), *Advances in Neural Information Processing Systems*, volume 35, pp. 28708–28720. Curran Associates, Inc., 2022. URL [https://proceedings.neurips.cc/paper\\_files/paper/2022/file/b89d5e209990b19e33b418e14f323998-Paper-Conference.pdf](https://proceedings.neurips.cc/paper_files/paper/2022/file/b89d5e209990b19e33b418e14f323998-Paper-Conference.pdf). 1
- iNaturalist 2021 competition dataset. iNaturalist 2021 competition dataset. [https://github.com/visipedia/inat\\_comp/tree/master/2021](https://github.com/visipedia/inat_comp/tree/master/2021), 2021. 25
- Georg B. Keller and Thomas D. Mrsic-Flogel. Predictive processing: A canonical cortical computation. *Neuron*, 100(2):424–435, Oct 2018. ISSN 0896-6273. doi:[10.1016/j.neuron.2018.10.003](https://doi.org/10.1016/j.neuron.2018.10.003). 3
- Simon Kornblith, Mohammad Norouzi, Honglak Lee, and Geoffrey Hinton. Similarity of neural network representations revisited. In *Proceedings of the 36th International Conference on Machine Learning (ICML)*, pp. 3519–3529, 2019. 37
- Hongyang Lei, Xiaolong Cheng, Qi Qin, Dan Wang, Huazhen Huang, Qingqing Gu, Yetao Wu, and Luo Ji. M3-JEPA: Multimodal alignment via multi-gate MoE based on the joint-embedding predictive architecture. In *Proceedings of the 42nd International Conference on Machine Learning (ICML)*. PMLR, 2025. URL <https://proceedings.mlr.press/v267/lei25b.html>. 1
- Michael A. Lepori, Alexia R. Tartaglino, Wai Keen Vong, Thomas Serre, Brenden M. Lake, and Ellie Pavlick. Beyond the doors of perception: Vision transformers represent relations between objects. In A. Globerson, L. Mackey, D. Belgrave, A. Fan, U. Paquet, J. Tomczak, and C. Zhang (eds.), *Advances in Neural Information Processing Systems*, volume 37, pp. 131503–131544. Curran Associates, Inc., 2024. doi:[10.52202/079017-4180](https://doi.org/10.52202/079017-4180). 3
- Zhe Li, Zhongwen Rao, Lujia Pan, Pengyun Wang, and Zenglin Xu. Ti-MAE: Self-supervised masked time series autoencoders. *arXiv preprint arXiv:2301.08871*, 2023. doi:[10.48550/arxiv.2301.08871](https://doi.org/10.48550/arxiv.2301.08871). 1
- Shentong Mo and Shengbang Tong. Connecting joint-embedding predictive architecture with contrastive self-supervised learning. In A. Globerson, L. Mackey, D. Belgrave, A. Fan, U. Paquet, J. Tomczak, and C. Zhang (eds.), *Advances in Neural Information Processing Systems*, volume 37, pp. 2348–2377. Curran Associates, Inc., 2024. doi:[10.52202/079017-0077](https://doi.org/10.52202/079017-0077). 10
- Kevin Kermani Nejad, Paul Anastasiades, Loreen Hertäg, and Rui Ponte Costa. Self-supervised predictive learning accounts for cortical layer-specificity. *Nature Communications*, 16(1):6178, Jul 2025. ISSN 2041-1723. doi:[10.1038/s41467-025-61399-5](https://doi.org/10.1038/s41467-025-61399-5). 3
- Yuqi Nie, Nam H. Nguyen, Phanwadee Sinthong, and Jayant Kalagnanam. A time series is worth 64 words: Long-term forecasting with transformers. In *The Eleventh International Conference on Learning Representations*, 2023. URL <https://openreview.net/forum?id=Jbdc0vT0col>. 1
- Maxime Oquab, Timothée Darcet, Théo Moutakanni, Huy V. Vo, Marc Szafraniec, Vasil Khalidov, Pierre Fernandez, Daniel Haziza, Francisco Massa, Alaaeldin El-Nouby, Mido Assran, Nicolas Ballas, Wojciech Galuba, Russell Howes, Po-Yao Huang, Shang-Wen Li, Ishan Misra, Michael Rabbat, Vasu Sharma, Gabriel Synnaeve, Hu Xu, Herve Jegou, Julien Mairal, Patrick Labatut, Armand Joulin, and Piotr Bojanowski. DINOv2: Learning robust visual features without supervision. *Transactions*

- on *Machine Learning Research*, 2024. ISSN 2835-8856. URL <https://openreview.net/forum?id=a68Sut6zFt>. Featured Certification. 10
- Namuk Park, Wonjae Kim, Byeongho Heo, Taekyung Kim, and Sangdoon Yun. What do self-supervised vision transformers learn? In *The Eleventh International Conference on Learning Representations*, 2023. URL <https://openreview.net/forum?id=azCKuYs74>. 3, 4
- Maithra Raghu, Thomas Unterthiner, Simon Kornblith, Chiyuan Zhang, and Alexey Dosovitskiy. Do vision transformers see like convolutional neural networks? In M. Ranzato, A. Beygelzimer, Y. Dauphin, P.S. Liang, and J. Wortman Vaughan (eds.), *Advances in Neural Information Processing Systems*, volume 34, pp. 12116–12128. Curran Associates, Inc., 2021. URL [https://proceedings.neurips.cc/paper\\_files/paper/2021/file/652cf38361a209088302ba2b8b7f51e0-Paper.pdf](https://proceedings.neurips.cc/paper_files/paper/2021/file/652cf38361a209088302ba2b8b7f51e0-Paper.pdf). 3, 4
- Rajesh P. N. Rao and Dana H. Ballard. Predictive coding in the visual cortex: a functional interpretation of some extra-classical receptive-field effects. *Nature Neuroscience*, 2(1):79–87, Jan 1999. ISSN 1546-1726. doi:10.1038/4580. 3
- Joséphine Raugel, Marc Szafraniec, Huy V. Vo, Camille Couprie, Patrick Labatut, Piotr Bojanowski, Valentin Wyart, and Jean-Rémi King. Disentangling the factors of convergence between brains and computer vision models. *arXiv preprint arXiv:2508.18226*, 2025. doi:10.48550/arxiv.2508.18226. 3
- Alain Riou, Stefan Lattner, Gaëtan Hadjeres, Michael Anslow, and Geoffroy Peeters. Stem-JEPA: A Joint-Embedding Predictive Architecture for Musical Stem Compatibility Estimation. In *Proceedings of the 25th International Society for Music Information Retrieval Conference*, San Francisco, nov 2024. ISMIR. 1
- Olga Russakovsky, Jia Deng, Hao Su, Jonathan Krause, Sanjeev Satheesh, Sean Ma, Zhiheng Huang, Andrej Karpathy, Aditya Khosla, Michael Bernstein, Alexander C. Berg, and Li Fei-Fei. ImageNet large scale visual recognition challenge. *International Journal of Computer Vision*, 115(3):211–252, Apr 2015. doi:10.1007/s11263-015-0816-y. 5
- Monireh Safari, Pablo Millan Arias, Scott C. Lowe, Lila Kari, Angel X. Chang, and Graham W. Taylor. Enhancing DNA foundation models to address masking inefficiencies. *arXiv preprint arXiv:2502.18405*, 2025. doi:10.48550/arxiv.2502.18405. 1
- Oriane Siméoni, Huy V. Vo, Maximilian Seitzer, Federico Baldassarre, Maxime Oquab, Cijo Jose, Vasil Khalidov, Marc Szafraniec, Seungeun Yi, Michaël Ramamonjisoa, Francisco Massa, Daniel Haziza, Luca Wehrstedt, Jianyuan Wang, Timothée Darcet, Théo Moutakanni, Leonel Sentana, Claire Roberts, Andrea Vedaldi, Jamie Tolan, John Brandt, Camille Couprie, Julien Mairal, Hervé Jégou, Patrick Labatut, and Piotr Bojanowski. DINOv3. *arXiv preprint arXiv:2508.10104*, 2025. doi:10.48550/arxiv.2508.10104. 1
- Robin Strudel, Ricardo Garcia, Ivan Laptev, and Cordelia Schmid. Segmenter: Transformer for semantic segmentation. In *Proceedings of the IEEE/CVF International Conference on Computer Vision (ICCV)*, pp. 7242–7252, 2021. doi:10.1109/ICCV48922.2021.00717. 6, 27
- Jianlin Su, Murtadha Ahmed, Yu Lu, Shengfeng Pan, Wen Bo, and Yunfeng Liu. RoFormer: Enhanced transformer with rotary position embedding. *Neurocomputing*, 568:127063, 2024. ISSN 0925-2312. doi:10.1016/j.neucom.2023.127063. 18
- Yingtian Tang, Abdulkadir Gokce, Khaled Jedoui Al-Karkari, Daniel Yamins, and Martin Schrimpf. Many-two-one: Diverse representations across visual pathways emerge from a single objective. *bioRxiv*, 2025. doi:10.1101/2025.07.22.664908. 3
- Hugo Thimonier, José Lucas De Melo Costa, Fabrice Popineau, Arpad Rimmel, and Bich-Liên Doan. T-JEPA: Augmentation-free self-supervised learning for tabular data. In *The Thirteenth International Conference on Learning Representations*, 2025. URL <https://openreview.net/forum?id=gx3LMRB15C>. 1
- Naftali Tishby, Fernando C. Pereira, and William Bialek. The information bottleneck method. In *Proceedings of the 37th Allerton Conference on Communication, Control, and Computing*, pp. 368–377, 1999. doi:10.48550/arXiv.physics/0004057. 4
- Ludovic Tuncay, Etienne Labbé, Emmanouil Benetos, and Thomas Pellegrini. Audio-JEPA: Joint-embedding predictive architecture for audio representation learning. *arXiv preprint arXiv:2507.02915*, 2025. doi:10.48550/arxiv.2507.02915. 1
- Aaron van den Oord, Yazhe Li, and Oriol Vinyals. Representation learning with contrastive predictive coding. *arXiv preprint arXiv:1807.03748*, 2018. doi:10.48550/arxiv.1807.03748. 10
- Grant Van Horn, Oisín Mac Aodha, Yang Song, Yin Cui, Chen Sun, Alex Shepard, Hartwig Adam, Pietro Perona, and Serge Belongie. The iNaturalist species classification and detection dataset. In *Proceedings of the IEEE Conference on Computer Vision and Pattern Recognition (CVPR)*, pp. 8769–8778, Los Alamitos, CA, USA, June 2018. IEEE Computer Society. doi:10.1109/CVPR.2018.00914. URL [https://openaccess.thecvf.com/content\\_cvpr\\_2018/papers/Van\\_Horn\\_The\\_iNaturalist\\_Species\\_CVPR\\_2018\\_paper.pdf](https://openaccess.thecvf.com/content_cvpr_2018/papers/Van_Horn_The_iNaturalist_Species_CVPR_2018_paper.pdf). 6
- Shashanka Venkataramanan, Valentinos Pariza, Mohammadreza Salehi, Lukas Knobel, Spyros Gidaris, Elias Ramzi, Andrei Bursuc, and Yuki M. Asano. Franca: Nested matryoshka clustering for scalable visual representation learning. *arXiv preprint arXiv:2507.14137*, 2025. doi:10.48550/arxiv.2507.14137. 1, 8, 10
- Martina G. Vilas, Timothy Schaumlöffel, and Gemma Roig. Analyzing vision transformers for image classification in class embedding space. In A. Oh, T. Naumann, A. Globerson, K. Saenko, M. Hardt, and S. Levine (eds.), *Advances in Neural Information Processing Systems*, volume 36, pp. 40030–40041. Curran Associates, Inc., 2023. URL <https://proceedings>.

- [neurips.cc/paper\\_files/paper/2023/file/7dd309df03d37643b96f5048b44da798-Paper-Conference.pdf](https://neurips.cc/paper_files/paper/2023/file/7dd309df03d37643b96f5048b44da798-Paper-Conference.pdf). 3
- Limin Wang, Bingkun Huang, Zhiyu Zhao, Zhan Tong, Yinan He, Yi Wang, Yali Wang, and Yu Qiao. VideoMAE V2: Scaling video masked autoencoders with dual masking. In *Proceedings of the IEEE/CVF Conference on Computer Vision and Pattern Recognition (CVPR)*, pp. 14549–14560, 2023. doi:10.1109/CVPR52729.2023.01398. 1
- Chen Wei, Haoqi Fan, Saining Xie, Chao-Yuan Wu, Alan Yuille, and Christoph Feichtenhofer. Masked feature prediction for self-supervised visual pre-training. In *Proceedings of the IEEE/CVF Conference on Computer Vision and Pattern Recognition (CVPR)*, pp. 14668–14678, 2022. doi:10.1109/CVPR52688.2022.01426. 9
- Junfei Xiao, Yutong Bai, Alan Yuille, and Zongwei Zhou. Delving into masked autoencoders for multi-label thorax disease classification. In *Proceedings of the IEEE/CVF Winter Conference on Applications of Computer Vision (WACV)*, pp. 3577–3589, 2023. doi:10.1109/WACV56688.2023.00358. 1
- Zhenda Xie, Zheng Zhang, Yue Cao, Yutong Lin, Jianmin Bao, Zhuliang Yao, Qi Dai, and Han Hu. SimMIM: A simple framework for masked image modeling. In *Proceedings of the IEEE/CVF Conference on Computer Vision and Pattern Recognition (CVPR)*, pp. 9643–9653, 2022. doi:10.1109/CVPR52688.2022.00943. 9
- Daniel L. K. Yamins and James J. DiCarlo. Using goal-driven deep learning models to understand sensory cortex. *Nature Neuroscience*, 19(3):356–365, Mar 2016. ISSN 1546-1726. doi:10.1038/nn.4244. 3
- Daniel L. K. Yamins, Ha Hong, Charles F. Cadieu, Ethan A. Solomon, Darren Seibert, and James J. DiCarlo. Performance-optimized hierarchical models predict neural responses in higher visual cortex. *Proceedings of the National Academy of Sciences*, 111(23):8619–8624, 2014. doi:10.1073/pnas.1403112111. 3
- Thomas Yerxa, Yilun Kuang, Eero Simoncelli, and SueYeon Chung. Learning efficient coding of natural images with maximum manifold capacity representations. In A. Oh, T. Naumann, A. Globerson, K. Saenko, M. Hardt, and S. Levine (eds.), *Advances in Neural Information Processing Systems*, volume 36, pp. 24103–24128. Curran Associates, Inc., 2023. URL [https://proceedings.neurips.cc/paper\\_files/paper/2023/file/4bc6e94f2308c888fb69626138a2633e-Paper-Conference.pdf](https://proceedings.neurips.cc/paper_files/paper/2023/file/4bc6e94f2308c888fb69626138a2633e-Paper-Conference.pdf). 10
- Goksenin Yuksel, Pierre Guetschel, Michael Tangermann, Marcel van Gerven, and Kiki van der Heijden. WavJEPa: Semantic learning unlocks robust audio foundation models for raw waveforms. *arXiv preprint arXiv:2509.23238*, 2025. doi:10.48550/arxiv.2509.23238. 1
- Jure Zbontar, Li Jing, Ishan Misra, Yann LeCun, and Stephane Deny. Barlow twins: Self-supervised learning via redundancy reduction. In Marina Meila and Tong Zhang (eds.), *Proceedings of the 38th International Conference on Machine Learning*, volume 139 of *Proceedings of Machine Learning Research*, pp. 12310–12320. PMLR, 18–24 Jul 2021. URL <https://proceedings.mlr.press/v139/zbontar21a.html>. 10
- Matthew D. Zeiler and Rob Fergus. Visualizing and understanding convolutional networks. In David Fleet, Tomas Pajdla, Bernt Schiele, and Tinne Tuytelaars (eds.), *European Conference on Computer Vision*, pp. 818–833, Cham, 2014. Springer International Publishing. doi:10.1007/978-3-319-10590-1\_53. 3
- Xiaohua Zhai, Joan Puigcerver, Alexander Kolesnikov, Pierre Ruysen, Carlos Riquelme, Mario Lucic, Josip Djolonga, André Susano Pinto, Maxim Neumann, Alexey Dosovitskiy, Lucas Beyer, Olivier Bachem, Michael Tschannen, Marcin Michalski, Olivier Bousquet, Sylvain Gelly, and Neil Houlsby. A large-scale study of representation learning with the visual task adaptation benchmark. *arXiv preprint arXiv:1910.04867*, 2019. doi:10.48550/arxiv.1910.04867. 6, 29
- Renrui Zhang, Ziyu Guo, Peng Gao, Rongyao Fang, Bin Zhao, Dong Wang, Yu Qiao, and Hongsheng Li. Point-M2AE: Multi-scale masked autoencoders for hierarchical point cloud pre-training. In S. Koyejo, S. Mohamed, A. Agarwal, D. Belgrave, K. Cho, and A. Oh (eds.), *Advances in Neural Information Processing Systems*, volume 35, pp. 27061–27074. Curran Associates, Inc., 2022. URL [https://proceedings.neurips.cc/paper\\_files/paper/2022/file/ad1d7a4df30a9c0c46b387815a774a84-Paper-Conference.pdf](https://proceedings.neurips.cc/paper_files/paper/2022/file/ad1d7a4df30a9c0c46b387815a774a84-Paper-Conference.pdf). 1
- Bolei Zhou, Aditya Khosla, Agata Lapedriza, Aude Oliva, and Antonio Torralba. Object detectors emerge in deep scene CNNs. In *International Conference on Learning Representations*, 2015. doi:10.48550/arxiv.1412.6856. 3
- Bolei Zhou, Hang Zhao, Xavier Puig, Sanja Fidler, Adela Barriuso, and Antonio Torralba. Scene parsing through ADE20K dataset. In *Proceedings of the IEEE/CVF Conference on Computer Vision and Pattern Recognition (CVPR)*, pp. 5122–5130, 2017. doi:10.1109/CVPR.2017.544. 6
- Jinghao Zhou, Chen Wei, Huiyu Wang, Wei Shen, Cihang Xie, Alan Yuille, and Tao Kong. Image BERT pre-training with online tokenizer. In *International Conference on Learning Representations*, 2022. URL <https://openreview.net/forum?id=ydopy-e6Dg>. 9, 10
- Lei Zhou, Huidong Liu, Joseph Bae, Junjun He, Dimitris Samaras, and Prateek Prasanna. Self pre-training with masked autoencoders for medical image classification and segmentation. In *Proceedings of the IEEE 20th International Symposium on Biomedical Imaging (ISBI)*, pp. 1–6. IEEE, 2023. doi:10.1109/ISBI53787.2023.10230477. 1

# Appendices

<b>A</b>	<b>Additional illustrative experiments</b>	<b>17</b>
<b>B</b>	<b>Pretraining hyperparameters</b>	<b>17</b>
<b>C</b>	<b>Masking strategy</b>	<b>19</b>
C.1	Seeding the RNG for the batch . . . . .	20
C.2	Sampling height/width of predictor masks . . . . .	20
C.3	Sampling height/width of background masks . . . . .	22
C.4	Sampling the placement of masks . . . . .	22
C.5	Encoder mask truncation strategy . . . . .	23
<b>D</b>	<b>No-forward MSE loss function</b>	<b>23</b>
<b>E</b>	<b>Evaluation methodology</b>	<b>25</b>
E.1	Image classification (IN-1k and iNat21) . . . . .	25
E.2	Semantic segmentation (ADE20K and Cityscapes) . . . . .	26
<b>F</b>	<b>Additional evaluations</b>	<b>28</b>
F.1	Variance across random seeds . . . . .	28
F.2	Fine-tuned models . . . . .	28
F.3	VTAB classification . . . . .	29
<b>G</b>	<b>Additional ablations</b>	<b>32</b>
G.1	Preliminary hyperparameters . . . . .	32
G.2	Choice of target layers . . . . .	32
G.3	Masking hyperparameter sensitivity . . . . .	34
<b>H</b>	<b>Additional experiments</b>	<b>35</b>
H.1	Predicting register tokens . . . . .	35
H.2	Using different targets for each mask . . . . .	35
H.3	Using a cross-attention predictor with Bootleg . . . . .	36
H.4	Jointly standardizing targets . . . . .	36
<b>I</b>	<b>Representational analysis</b>	<b>37</b>
I.1	Inter-layer similarity . . . . .	37
I.2	Distillation target layer analysis . . . . .	37
I.3	Spatial correlation structure . . . . .	37

## A Additional illustrative experiments

To accompany Sec. 3.2, we present the zoomed out figure for the MAE config. This figure shows the performance of ViT-S with unmodified MAE config, except instead of predicting the pixels in the input image, we predict the representation from a hidden layer within an EMA teacher (blue line). In this zoomed out version of the plot (Fig. 3), we can see the severity of the collapse in performance when doing hidden-self-distillation of blocks 5–11 and using the unmodified MAE config. Other work has indicated that using the L1 loss provides increased stability compared to using L2 or smooth-L1 (Bardes et al., 2024; Assran et al., 2025), however we did not find evidence that this could alleviate our issue (Fig. 3, yellow line).

For ViT-B, the drop in performance when using deeper hidden layers as the distillation target was more gradual (Fig. 3, right panel). Since ViT-B is wider than ViT-S, this, albeit weakly, suggests that a higher-dimensional target vector may help with training stability.

## B Pretraining hyperparameters

We selected the hyperparameters for pretraining Bootleg in a multi-step process of iterative refinement.

Initially, we referred to the hyperparameters used in MAE (He et al., 2022) and I-JEPA (Assran et al., 2023). In our preliminary experiments (*cf.* Fig. 2, “Bridging I-JEPA and MAE with targets across hidden layers”, of the main paper), we found training using the MAE hyperparameter configuration with the I-JEPA masking strategy and a hidden target for self-distillation outperformed similar experiments using the I-JEPA hyperparameter configuration. We thus initialized our hyperparameter configuration with that of MAE. Through a series of preliminary experiments conducted with ViT-S, 300 ep., we considered changing hyperparameters to that of I-JEPA or V-JEPA (Bardes et al., 2024), resulting in the hyperparameters shown in Table 18. We additionally considered adding register tokens (Darcet et al., 2024) since this had been shown to be highly beneficial for networks pretrained with DINO (Darcet et al., 2024). We found adding (separate) registers to each of the encoder and predictor networks was beneficial.

We then conducted a series of line searches with ViT-S, 300 ep., on the predictor size, learning rate schedule, weight decay, and number of warm-up steps. To assess the scaling of the predictor size relative to the encoder size, we conducted a small number of experiments with ViT-B and -L encoders, varying both the width and depth of the encoder. To assess the learning rate, which may vary depending on model size, we conducted limited experiments on ViT-B and -L using the schedule established with ViT-S. Our final hyperparameters are shown in Table 6. We found that a larger crop size, longer LR warmup duration, and higher maximum and minimum LR values improved performance of the resulting model. We scale the warmup duration based on the total number of epochs,  $E$ , as  $E_{\text{wu}} = 33 + 0.12 E$ .

We changed the model seed used between each round of our hparam search to avoid overfitting to a specific model. The final evaluations shown in the main table were performed on models trained from scratch using a fresh seed which had not been included in the hyperparameter search.

Some hyperparameters vary between model sizes. The resulting values are shown in Table 7. We use a ViT

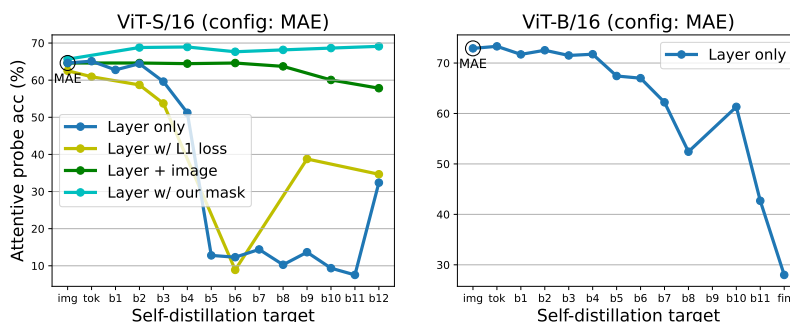


Figure 3: Accompanies Fig. 2 of the main text. Bridging I-JEPA and MAE with targets across hidden layers. *Left:* As in Fig. 2 of the main text, we train ViT-S using with MAE, except we add EMA for self-distillation and change the target to be a hidden layer of the EMA model instead of the input pixels (blue) or in addition to the image pixels (green). We compare to a single target with our masking strategy (cyan), and to a single target but using the L1 loss (yellow). Using the L1 loss is insufficient to prevent training instabilities when using deeper layers as targets. *Right:* Similar, but for ViT-B with MAE config.

Table 6: Hyperparameter configuration comparison between Bootleg, I-JEPA, MAE for ViT-B/16. Learning rate (LR) values are tabulated for a batch size of 2048 samples, and linearly scaled to the batch size used for training. Mask seen rate and target rate are empirically estimated (mean  $\pm$  stdev) for I-JEPA and Bootleg with a batch size per GPU of 256.

	Hyperparameter	MAE	I-JEPA	Bootleg (ours)
Encoder	Architecture	ViT-B/16	ViT-B/16	ViT-B/16
	Depth	12	12	12
	Width	768	768	768
	Attention heads	12	12	12
	Patch size	16	16	16
	CLS tokens	1	0	1
	Register tokens	0	0	4
Predictor	Depth	8	6	10
	Width	512	384	384
	Attention heads	16	12	16
	Register tokens	0	0	4
Data	Transforms	RandCrop(0.2, 1.0) + Hflip	RandCrop(0.3, 1.0)	RandCrop(0.35, 1.0) + Hflip
	Interpolation	Bicubic	Bilinear	Bicubic
	Input size	224 $\times$ 224	224 $\times$ 224	224 $\times$ 224
Masking	Strategy	Uniform random	4 rectangular blocks	4 rectangular blocks
	Mask seen rate	0.25	0.243 $\pm$ 0.037	0.292 $\pm$ 0.069
	Mask target rate	0.75	0.445 $\pm$ 0.070	0.475 $\pm$ 0.076
Training	Target(s)	Image pixels	Final (block 12) output	Block 1, 4, 8, 12 outputs
	Target standardization	Z-score	Z-score	Z-score
	Target length	768	768	3072
	Loss	Mean squared error	Smooth L1	Mean squared error
	Optimizer	AdamW( $\beta=(0.9, 0.95)$ )	AdamW( $\beta=(0.9, 0.999)$ )	AdamW( $\beta=(0.9, 0.95)$ )
	EMA initial	N/A	0.996	0.9985
	EMA final	N/A	1.0	0.9985
	LR schedule	Cosine annealing	Cosine annealing	Cosine annealing
	LR schedule warmup	40 epochs	40 epochs	105 epochs
	LR initial	0.0	0.0002	0.00003
	LR maximum	0.0012	0.001	0.003
	LR final	0.0	0.000001	0.00003
	WD initial	0.05	0.04	0.05
	WD final	0.05	0.40	0.05
	Schedule stretch	1.0	1.0	1.0
	Batch size	4096	2048	2048
Num epochs	1600	600	600	

predictor of depth 10 with width equal to half that of the encoder, with heads equal to same as the encoder with a minimum of 16 heads. We found ViT-S needed a higher initial and final LR (1/30 of the maximum) than ViT-B and -L (1/100 of the maximum LR).

Our results include ViT-S models, which is outside the original training recipes of MAE and I-JEPA, hence we additionally share the configs we used for these in Table 7. For MAE, we follow the ViT-S recipe of (Fu et al., 2025). For I-JEPA, we halve the width of the predictor to maintain the same capacity relative to the encoder as used for ViT-B, and let the number of heads equal that of the encoder following the rule from I-JEPA (Assran et al., 2023).

Note that in preliminary experiments, we also considered replacing the absolute position embeddings with rotary position embeddings (RoPE) (Su et al., 2024) as used in V-JEPA-2 (Assran et al., 2025). We found RoPE was beneficial when not using register tokens, with a comparable effect size to adding register tokens, but using both at once was anti-synergistic. We suspect this is because the unrotated global tokens embeddings are handled in the same way as one of the patch tokens (either the top-left corner, or the centre of the image, depending on the RoPE vector initialization strategy). This effectively co-locates the CLS token and all four register tokens at a position within the image, potentially also colliding with one of the patch tokens, which makes it difficult for the attention heads to chose to address the register tokens. Furthermore, since we use five global tokens and mask the patch tokens presented to the encoder, the model will see 13 times as many global tokens as patch tokens at the position for which they collide. Since RoPE had a much higher compute burden (around +30%) compared to adding registers (negligible), we chose to use register tokens with 2d sin-cos absolute position embeddings. This

Table 7: Hyperparameter changes across encoder sizes ViT-S, -B, -L for MAE, I-JEPA, and Bootleg models. Learning rate (LR) values are tabulated for a batch size of 2048 samples, and linearly scaled to the batch size used for training.

Hyperparameter		MAE			I-JEPA			Bootleg (ours)		
		ViT-S	ViT-B	ViT-L	ViT-S	ViT-B	ViT-L	ViT-S	ViT-B	ViT-L
Encoder	Depth	12	12	24	12	12	24	12	12	24
	Width	384	768	1024	384	768	1024	384	768	1024
	Attention heads	6	12	16	6	12	16	6	12	16
	Patch size	16	16	16	16	16	16	16	16	16
	CLS tokens	1	1	1	0	0	0	1	1	1
Predictor	Register tokens	0	0	0	0	0	0	4	4	4
	Depth	8	8	8	6	6	12	10	10	10
	Width	256	512	512	192	384	384	192	384	512
	Attention heads	8	16	16	6	12	16	16	16	16
	Register tokens	0	0	0	0	0	0	4	4	4
Training	Target(s)	Input	Input	Input	Final	Final	Final	b1,4,8,12	b1,4,8,12	b1,4,8,12,16,20,24
	Target length	384	768	1024	384	768	1024	1536	3072	7168
	LR initial	0.0	0.0	0.0	2e-4	2e-4	2e-4	1e-4	3e-5	3e-5
	LR maximum	1.2e-3	1.2e-3	1.2e-3	1e-3	1e-3	1e-3	3e-3	3e-3	3e-3
	LR final	0.0	0.0	0.0	1e-6	1e-6	1e-6	1e-4	3e-5	3e-5

also allows us to better compare with our benchmark models, since MAE, CrossMAE, data2vec2, and I-JEPA all use absolute position embeddings.

## C Masking strategy

As mentioned in Sec. 4, our masking strategy is conceptually similar to that of I-JEPA, with only improvements in technical details and implementation. In this section, we describe this masking strategy, and highlight the improvements in our implementation compared to I-JEPA.

**Overview** The total batch size of 2048 is processed by some number of distributed GPU workers. For example, with 8 GPU workers, each GPU worker will process 256 samples. For a given GPU worker’s batch of samples, we generate masks using the same general process for both Bootleg and I-JEPA:

1. Choose a seed to use for the random number generator (RNG) for the masks in this worker’s batch.
2. Sample the height and width to use for the predictor mask rectangles:  $(p_h, p_w)$ . The same size is used for all four predictor mask rectangle across the worker’s batch.
3. Sample the height and width to use for the background mask:  $(b_h, b_w)$ . The same size is used for all background masks across the worker’s batch.
4. For each image in the batch, sample its mask positions:
  - (a) For each of the four predictor mask rectangles, sample their placement:  $p_{j,x}^{(i)}, p_{j,y}^{(i)}$ .
  - (b) For the background mask, sample its placement:  $b_x^{(i)}, b_y^{(i)}$ .
  - (c) Let the visible mask be the intersection between the background mask and the complement of the predictor mask rectangles:  $v^{(i)} := b^{(i)} \setminus (p_1^{(i)} \cup p_2^{(i)} \cup p_3^{(i)} \cup p_4^{(i)})$
5. For GPU efficiency, all visible masks need to be the same length. Truncate all the visible masks to the length of the shortest visible mask within the GPU worker’s batch.

Note that we need to truncate the visible masks because the four predictor mask rectangles will overlap by a random amount. For some samples in the worker’s batch, there will be very little overlap, resulting in the visible mask having fewer elements. Whereas for other samples in the worker’s batch, there will be a lot of overlap (potentially all four predictor mask rectangles overlap entirely), which would mean more visible tokens for these samples without truncation. The predictor mask rectangles are always the same size within the worker’s batch and so do not need truncation to have the same length.

As presented below, we make technical improvements to *all* steps within this pipeline. The most significant of

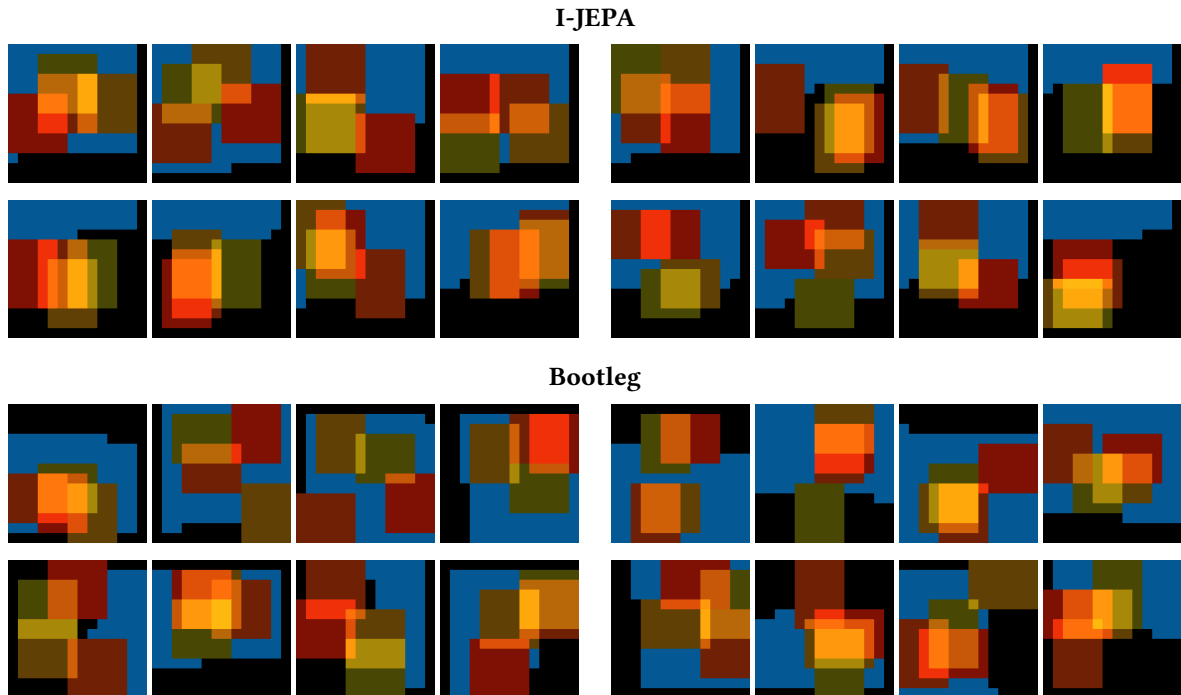


Figure 4: Sample masks generated by I-JEPA and Bootleg’s masking strategies. Visible tokens are shown in blue. Prediction masks are shown in green/yellow/orange/red with one colour per mask rectangle. These prediction masks can overlap, leading to brighter shades of orange/yellow. Unused tokens (seen by the teacher-encoder, but not by either the student-encoder or predictor) are shown in black. For both I-JEPA and Bootleg, we show samples from worker-batches of 256 samples, generated with seeds 0,1,2,3. We show the first 4 examples from each batch (grouped horizontally). These samples illustrate how the visible tokens (blue) are always at the top of the image for I-JEPA’s masking, but are better distributed for Bootleg’s masks.

these improvements is in the visible token truncation strategy.

### C.1 Seeding the RNG for the batch

For reproducibility of experiments, we want to use a fixed RNG seed. Note that there is a hierarchy to the processes: (1) a main GPU worker at rank 0, responsible for collecting gradients and saving checkpoints, (2) the set of GPU workers with ranks e.g. 0–7, which may be running on the same or different nodes/machines to one another, (3) the CPU workers responsible for collating the batches of data, e.g. 12 per GPU worker.

In I-JEPA’s code, the global seed is set to 0. This is used to sample the random weights for the model, and the seed is set to 0 on [every GPU worker](#). To ensure each CPU worker uses a different seed from the others for the operations in its batch, `multiprocessing.Value` is used so the seed is shared across the CPU workers. However, since the GPU seed is the same, the set of seeds for the CPU workers for one GPU worker are the same as for every other GPU worker. This results in redundancy in the generated masks across the total batch, distributed across the GPU workers. (There is actually a race-condition in the dataloader workers, which leads to these shared-mask batches being desynchronized across steps, but the same set masks are used over a small number of steps equal to the number of CPU workers per GPU.)

In Bootleg’s implementation, we use a different seed for each GPU worker, which ensures the random crop data transform used differs across GPU workers, unlike in I-JEPA’s codebase. For reproducibility across pre-empted runs, we map the global seed, sample index, and epoch number to a seed to use for each specific presentation stimulus. Similarly, the CPU workers use seeds for their mask generation which are mapped from the global seed, global batch index, and epoch number. This ensures the set of masks generated are unique for each batch on each GPU worker, across all global CPU workers.

### C.2 Sampling height/width of predictor masks

The range of mask height and width values to sample are parametrized by a minimum/maximum block size, and minimum/maximum aspect ratio. Due to a bug in the I-JEPA code, the [same random number](#) was used to select the aspect ratio as the block size, resulting in correlation between the two. Consequently, small masks are always

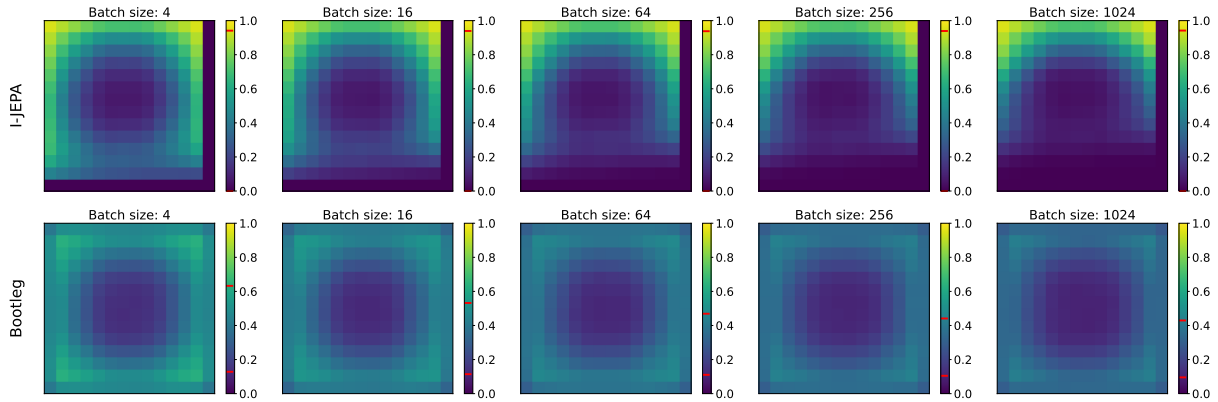


Figure 5: Rates at which each token position within the  $14 \times 14$  grid is visible and presented to the student-encoder. Top row: I-JEPA masking. Bottom row: Bootleg masking. We show the change in visibility of the tokens as the per-GPU batch size is increased from 4 (left) to 1024 (right). Red marks on the colorbars indicate the least and most frequent any token is visible for a given plot. Note that token visibility is more consistent across space (a flatter distribution) for Bootleg masks. The I-JEPA masks omit the bottom row and right column entirely, rarely present the centre of the image, and last-in-first-out truncation leads to the bottom four rows being seldom presented when the per-GPU batch size is larger.

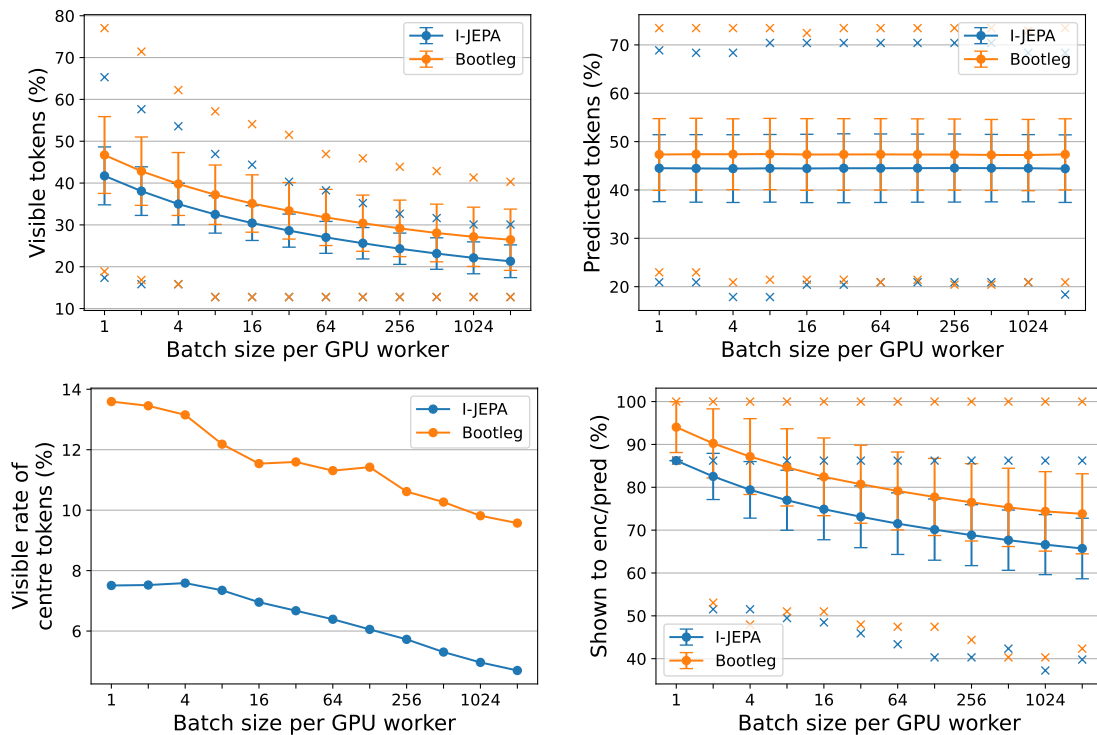


Figure 6: Token occurrence rates versus per-GPU batch size for I-JEPA and Bootleg masking strategies. Due to stochastic overlap of the predictor masks, the visible tokens need to be truncated to be the same length across all samples on the same GPU. Top left: Fraction of tokens which are visible (shown to the encoder) decreases as the batch size increases. This is because the target length for the visible tokens is the minimum size of the complement of the predictor masks within over all samples in the batch for the GPU worker, and a larger per-GPU batch size leads to more opportunities to generate four predictor rectangles with minimal overlap. Top right: Fraction of tokens predicted at least once across all masked out tokens per sample. Bottom left: Average fraction across the four centre tokens for the rate at which they are visible. Centre tokens infrequently visible for I-JEPA and are visible twice as often for Bootleg. Bottom right: Fraction of tokens within each image used either as a visible token passed to the encoder, or as a target token whose prediction loss is used to update the model. Due to random overlap and truncation, not all patch tokens are used for at least one task, reducing the efficiency of training. For each panel, the standard deviation is shown with error bars, and the min/max values with crosses.

more landscape and large masks are always more portrait (see Table 8).

In Bootleg, we fix this bug so size and aspect ratio are sampled independently. However, when fixing this, the distribution of mask sizes sampled in practice changed. We thus refined the requested range of mask sizes from  $[0.15, 0.20]$  (defined as a fraction of the image area) to a narrower range of  $[0.16, 0.183]$ , which better reflected the range actually being sampled by I-JEPA (see Table 8 for a comparison of the sampled sizes with this parameter).

Additionally, the mask rectangles for Bootleg use alternating aspect ratios (by swapping the height and width after generating each mask) to increase diversity of masks used for each sample within the worker’s batch. This change also reduces the range of overlap amounts for the masks, since (when the aspect ratio is not square) it is impossible for all masks to overlap completely if two of them are oriented rotated  $90^\circ$  from the two. This increases the consistency of the mask generation and reduces the amount of truncation that needs to be applied to the visible tokens.

Table 8: Distribution of shapes of prediction target mask rectangles for I-JEPA and Bootleg. We assume a  $14 \times 14$  grid of tokens (equivalent to a  $224 \times 224$  image with  $16 \times 16$  patch size), and sample 1 million mask sizes.

(h, w)	Area	Aspect	Rate (%)	
			I-JEPA	Bootleg
(5, 6)	30	0.83	26.5	18.8
(6, 5)	30	1.20	12.6	18.7
(5, 7)	35	0.71	0.0	20.0
(7, 5)	35	1.40	36.5	20.1
(6, 6)	36	1.00	21.8	22.4
(5, 8)	40	0.63	0.0	0.0
(8, 5)	40	1.60	2.6	0.0

### C.3 Sampling height/width of background masks

In I-JEPA, the background mask is supposed to be randomly sampled from  $[0.85, 1.0]$  of the total patches in the image, with an aspect ratio always set to 1.0. For a  $224 \times 224$  image with  $16 \times 16$  pixels per patches, this means a grid of  $14 \times 14$  patch tokens, with the background mask being either all  $14 \times 14$ , or a  $13 \times 13$  square within it. However, due to an off-by-one error in the I-JEPA code, the background mask is capped at one token narrower than the image in both height and width, [as pointed out by George Hu](#), meaning the background mask is always a  $13 \times 13$  square.

In Bootleg, we fix this bug. Our background mask is randomly sampled to be either a  $13 \times 13$  square of patch tokens, or the full  $14 \times 14$  square grid.

### C.4 Sampling the placement of masks

In I-JEPA, the mask placement has an off-by-one error, meaning masks are randomly placed somewhere in the upper-left  $13 \times 13$  square of patch tokens, [as pointed out by Jack Wilkie](#). When combined with Appx. C.3, “*Sampling height/width of background masks*”, this means the background mask for I-JEPA is always the  $13 \times 13$  square in the top-left corner. Consequently, the I-JEPA student-encoder never sees the right-most column or bottom-most row of image patches, which amounts to 14% of the image, and the predictor is never asked to predict these tokens either.

In Bootleg, we fix this bug and sample mask locations uniformly across space while restricting the mask to be contiguous. However, note that this sampling strategy still means prediction masks are less likely to be in the corners of the image and are more likely to be nearer the middle. This is because there is only one valid position for a rectangular mask to be in any given corner of the image, but many positions allow it to overlap with the middle of the image. Consequently, our student-encoder sees the edges of the image more often than it sees the middle of the image, and predicts the middle of the image more often than the edges. It is unclear whether this centre/surround bias is an advantageous component of the masking strategy.

Additionally, note that because the four masks are always sized at least  $5 \times 6$ , random placement leaves them unlikely to be placed somewhere which does not overlap with the centre patch tokens within the image. Increasing the background from the top-left  $13 \times 13$  grid to  $14 \times 14$  greatly increases the number of placements which do

not overlap with the centre of the image, resulting in an increased rate at which these tokens are visible (see Fig. 6).

### C.5 Encoder mask truncation strategy

We truncate the visible masks to length  $V' = \min_i |v^{(i)}|$ , the minimum length within the worker’s batch. The visible mask tokens are encoded as a list ordered by their index in row-column order, *i.e.* first the top row (from left to right), then the second row (from left to right), *etc.* In I-JEPA, the visible masks are truncated by [keeping the first](#)  $V'$  tokens within this sorted order. Only a minority of samples within a worker’s batch will have minimal overlap between the mask rectangles, so most samples undergo some amount of truncation to the list of visible tokens. This means the context seen by the student-encoder is biased towards the top of the image (which is never truncated), with the student very rarely seeing any of the bottom three rows of image token patches (which are frequently truncated), as shown in Fig. 5 and illustrated in Fig. 4.

In Bootleg, we fix this issue by randomizing the edge from which the truncation is performed. We randomly select one of the four corners of the grid, and randomly select an orientation (rows or columns) and truncate from that corner inwards. The edge and orientation is independently selected for each sample within the worker’s batch.

We considered other truncation strategies, such as removing a token with a uniform random distribution across all visible tokens or across all visible tokens at the edge of the image, but found it was better to remove tokens from one randomly selected edge instead.

## D No-forward MSE loss function

Our hidden-self-distillation method, Bootleg, uses an increased number of training targets compared to MAE or I-JEPA. We found an increased proportion of experiment run-time was devoted to computing the loss, which increased the more distillation targets were used. For our proposed methodology, in which the output from every fourth transformer block is used as a self-distillation target, the computational overhead of the increased targets is not much (4 times as much as for I-JEPA; less than 2% of total runtime). But for some of our preliminary explorations (see Appx. G.2.1) using the output and residuals from every block (9 times more targets than Bootleg, 36 times more than I-JEPA), the loss computation was significant (11% of total runtime), motivating us to find a solution.

Note that we do not need to know the loss value on every step—periodic evaluation and logging of the loss is sufficient for tracking training—we only need to compute the loss on each step so we can compute gradients. So to reduce the amount of compute spent during training, we propose and implemented a no-forward version of the MSE loss, `MSELossNoForward`, shown in Listing 1. This method skips the forward computation of the loss, returning a dummy value, but will compute the gradient of the loss to return the same values in the backward pass as `MSELoss`. It can be used in the compute graph like the conventional `MSELoss`, with downstream operations, such as scaling the loss by the world size or with a `GradScaler`, fed back into the backward pass of `MSELossNoForward`.

In practice, we accompany this with a separate forward computation of the MSE loss spaced at regular intervals (*e.g.* every twenty steps) for monitoring purposes.

Listing 1: Pytorch implementation of no-forward, backward-only, mean squared error (MSE) loss function.

```
1 class MSELossNoForward(torch.autograd.Function):
2     @staticmethod
3     def forward(
4         ctx, input: torch.Tensor, target: torch.Tensor, reduction: str = "mean"
5     ):
6         # Compute the difference between input and target and save it.
7         # This computation is only needed for the backward pass, but doing
8         # it now halves the memory requirement we need in the context.
9         ctx.save_for_backward(input - target)
10        ctx.reduction = reduction
11        # Return a dummy scalar tensor (no forward computation).
12        # Match the device and dtype of input.
13        dummy = input.new_zeros((), requires_grad=True)
14        return dummy
15
16    @staticmethod
17    def backward(ctx, grad_output):
18        # Recover difference between input and target, saved in forward pass
19        difference = ctx.saved_tensors[0]
20        reduction = ctx.reduction
21        # Constant scaling of 2.0 comes from derivative of mean squared error.
22        scaling = 2.0
23        # If we are simulating taking the mean, scale against the number of
24        # elements being averaged.
25        if reduction == "mean":
26            scaling /= difference.numel()
27        # Usually grad_output is 1.0/world_size, but may differ if using a
28        # GradScaler. Multiply grad_output by the constant term.
29        grad_output *= scaling
30        # Chain rule: multiply upstream gradient by (input - target).
31        grad_input = grad_output * difference
32        grad_target = None # No gradient w.r.t. target
33        grad_reduction = None
34        return grad_input, grad_target, grad_reduction
```

## E Evaluation methodology

### E.1 Image classification (IN-1k and iNat21)

#### E.1.1 Frozen probes

As described in Sec. 5.1, we evaluated the pretrained networks by using probes of the frozen encoder. Since the majority of compute is spent passing the images through the frozen encoder, which is the same for all probes, we perform a simultaneous hyperparameter sweep on each probe type, with 25 hyperparameters considered for each.

We consider four types of frozen probes. Firstly, we consider the long-standing linear probe of the average patch embeddings (column “**Patch**” in tables). We discard the CLS token and register tokens, take the average of the patch embeddings, apply batch norm, and a single learnable linear layer to predict the IN-1k classes. Secondly, we consider the performance of a linear probe of the CLS token embedding (column “**CLS**” in tables). We discard the patch tokens and register tokens, add a LayerNorm layer without trainable parameters, and train a single learnable linear layer on the CLS token embedding. Thirdly, we consider the performance of a minimal attentive probe (column “**X-Attn**” in tables). We keep the patch, CLS, and any register embeddings produced by the model; these are passed to a cross-attention block with a single learnable query vector, followed by a single linear head only. We use the same width and number of attention heads as in the pretrained ViT. Finally, we consider the performance of a non-linear attentive probe (column “**X-Blk**” in tables). This was performed following the implementation in V-JEPA (Bardes et al., 2024; Assran et al., 2025); the method is the same as X-Attn, except there is an MLP-block between the attention layer and the linear head.

We train the probes with a batch size of 1024 on either the IN-1k train set or iNat21 train set (iNaturalist 2021 competition dataset) for 20 epochs. (As iNat21 is around twice as large as IN-1k, this results in around twice as many training steps for its probes.) Training data is augmented through (1) random crops, sized (0.3, 1.0) of the original image and random stretch aspect ratio in the range 3:4 to 4:3, which are resized to 224×224 pixels with bicubic interpolation; (2) random horizontal flips with  $p = 0.5$ ; (3) and random colour jitter of up to 0.4 for brightness, contrast, and saturation. See Table 9.

The training (learning rate and weight decay) hyperparameters we considered are a 5×5 grid of logarithmic spaced values:  $\eta_{\max} \in [0.0005, 0.001, 0.002, 0.004, 0.008]$  and  $\lambda \in [0.0005, 0.001, 0.002, 0.004, 0.008]$ , respectively.

The performance of each probe is evaluated on the IN-1k/iNat21 validation set, with an 87.5% centre crop (resize to 256×256, then crop to 224×224). For each of the five probe types, we report the best result across the 25 training hyperparameters considered.

Table 9: Hyperparameter configuration for IN-1k classification probes.

	Hyperparameter	Value	
Encoder	Drop path	0.0	
Data	Input size	224×224	
	Cropping	RandCrop(0.3, 1.0)	
	Stretch	(3/4, 4/3)	
	Interpolation	Bicubic	
	Transforms	HFlip( $p=0.5$ )	
		ColorJitter(0.4)	
Training	Loss	Cross-entropy	
	Label smoothing	0.0	
	Optimizer	AdamW( $\beta=(0.9, 0.999)$ )	
	LR schedule	Cosine decay	
	LR schedule warmup	5 epochs	
	LR initial	0.0	
	LR maximum	$0.0005 \leq \eta_{\max} \leq 0.0080$	
	LR final	0.0	
	WD	$0.0005 \leq \lambda \leq 0.0080$	
	Batch size	1024	
	Epochs	20	

### E.1.2 Fine-tuning

We fine-tuned the pretrained models on IN-1k using either the full labels, or a 1% subset of the labels as described below.

Our methodology for full-fine tuning on IN-1k follows that recommended in the MAE GitHub repository and used by CrossMAE (Fu et al., 2025). The fine-tuning hyperparameters are detailed in Table 10.

Table 10: Hyperparameter configuration for IN-1k classification fine-tuning. Learning rate (LR) reference values are shown relative to a batch size of 256 and linearly scaled for the actual batch size. For 1% fine-tuning, we sweep five LR values and report the best; the swept ranges are shown.

		100% Full FT		1% Low-shot	
Hyperparameter		ViT-S,B	ViT-L	Full	LoRA
Encoder	Drop path	0.1	0.2	0.0	0.0
Data	Input size	224	224	224	224
	Interpolation	Bicubic	Bicubic	Bicubic	Bicubic
	HFlip	$p=0.5$	$p=0.5$	$p=0.5$	$p=0.5$
	Transforms	RandAug	RandAug	RandAug	RandAug
	RandErasure	$p=0.25$	$p=0.25$	$p=0$	$p=0$
	Subset	100%	100%	1%	1%
Training	Loss	CE	CE	CE	CE
	Label smoothing	0.1	0.1	0.1	0.1
	MixUp	0.8	0.8	0.0	0.0
	MixUp / CutMix	1.0	1.0	0.0	0.0
	Optimizer	AdamW	AdamW	AdamW	AdamW
	LR schedule	Cosine	Cosine	Cosine	Cosine
	Warmup	5 ep	5 ep	5 ep	5 ep
	LR initial	0.0	0.0	0.0	0.0
	LR ref (per 256 samp)	$5\times 10^{-4}$	$1\times 10^{-3}$	$[5\times 10^{-6}, 5\times 10^{-4}]$	$[1.5\times 10^{-6}, 1.5\times 10^{-3}]$
	LR final	$2.5\times 10^{-7}$	$2.5\times 10^{-7}$	0.0	0.0
	LR layer decay	0.65	0.75	0.75	1.0
	Weight decay	0.05	0.05	0.05	0.05
	Batch size	1024	1024	512	512
	Epochs	100	50	50	50
LoRA	Rank	full	full	full	8
	$\alpha$	N/A	N/A	N/A	16
	Dropout	N/A	N/A	N/A	0.05
	Targets	all	all	all	qkv, proj, mlp
	Train norms	✓	✓	✓	✓

We performed low-shot fine-tuning on 1% of IN-1k using the subset proposed by SimCLR (Chen et al., 2020a) and the methodology from I-JEPA (Assran et al., 2023). We adapted the methodology to sweep over five maximum learning rates,  $\eta_{\max} \in [5\times 10^{-6}, 1.5\times 10^{-5}, 5\times 10^{-5}, 1.5\times 10^{-4}, 5\times 10^{-4}]$ , and report the best performance over these learning rates.

We additionally evaluated the models at low-rank (parameter efficient) fine-tuning. For this we use the LoRA methodology (Hu et al., 2022) with rank = 8 and  $\alpha = 16$ . We fine-tune the attention QKV weights, attention projector, and MLP weights from every block on the 1% low-shot subset of IN-1k. Learning rates were swept over  $\eta_{\max} \in [1.5\times 10^{-5}, 5\times 10^{-5}, 1.5\times 10^{-4}, 5\times 10^{-4}, 1.5\times 10^{-3}]$ , and we report the best performance over these learning rates.

All fine-tuned models were evaluated on IN-1k validation set, with an 87.5% centre crop (resize to  $256\times 256$ , then crop to  $224\times 224$ ). Results are shown in Appx. F.2.

## E.2 Semantic segmentation (ADE20K and Cityscapes)

### E.2.1 Frozen probes – kNN

We evaluated the pretrained models’ representation of semantic information at the patch level with probes on the pretrained models using the kNN methodology from CAPI (Darcet et al., 2025). For this probe, images from the training partition are encoded without augmentations. The embeddings and pixel-wise segmentation labels for each patch token form the kNN training set. Inference is performed by finding the  $k$  nearest neighbours for

each patch in the image, and then for each pixel in the patch predicting the most common label across that pixel location in the  $k$  neighbours. We sweep 4 neighbourhood sizes  $k \in [1, 3, 10, 30]$ , using both cosine and L2 distance metrics.

### E.2.2 Frozen probes – Lin and Blk

We evaluated the pretrained models’ representation of semantic information at the pixel level using probes on the pretrained models with a Segmenter (Strudel et al., 2021) head trained atop the frozen backbone. We consider two heads, trained separately. “**Lin**”, a linear projector from the patch embeddings to the Segmenter; or “**Blk**”, with one randomly initialized transformer block before the projector. Our training strategy is based on the BEiT evaluation methodology (Bao et al., 2022); we train for 128 epochs with a batch size of 64, and augment the data with random resized cropping, horizontal flips, cut-out, and colour jitter. For the linear projector, we halve the magnitude of the colour jitter.

We sweep 4 LR for each head type, and report the best performance. For Lin probes, we use  $\eta_{\max} \in [2.5 \times 10^{-4}, 7.5 \times 10^{-4}, 2.5 \times 10^{-3}, 7.5 \times 10^{-3}]$  for Blk we use  $\eta_{\max} \in [2.5 \times 10^{-5}, 7.5 \times 10^{-5}, 2.5 \times 10^{-4}, 7.5 \times 10^{-4}]$ . We empirically found these LR ranges were in the optimal range for the models considered. See Table 11.

All frozen evaluation was performed using images at  $224 \times 224$  resolution. As the pretrained model uses sinusoidal position embeddings at  $224 \times 224$  resolution ( $14 \times 14$  patches), it lacks the flexibility to correctly process other image sizes without retraining.

Table 11: Hyperparameter configuration for ADE20K segmentation frozen probes. We sweep 4 learning rates for each head type.

	Hyperparameter	Lin	Blk
Decoder	Type	MaskTransformer	MaskTransformer
	Depth	0 blocks	1 block
Data	Input size	224	224
	Cropping	RandScale(0.5, 2.0)	RandScale(0.5, 2.0)
	HFlip	$p=0.5$	$p=0.5$
	Cutout	$p=0.5$	$p=0.5$
	ColorJitter	$p=0.5$ (half mag.)	$p=0.5$
	Brightness	0.0625	0.125
	Contrast	0.25	0.5
	Saturation	0.25	0.5
Training	Hue	0.035	0.07
	Loss	CrossEntropy	CrossEntropy
	Label smoothing	0.0	0.0
	Optimizer	AdamW	AdamW
	LR schedule	Cosine	Cosine
	Warmup	5 epochs	5 epochs
	LR initial	0.0	0.0
	LR max (per 256 samp)	$2.5 \times 10^{-4} \leq \eta_{\max} \leq 7.5 \times 10^{-3}$	$2.5 \times 10^{-5} \leq \eta_{\max} \leq 7.5 \times 10^{-4}$
	LR final	0.0	0.0
	Weight decay	0.0001	0.05
	Batch size	64	64
	Epochs	128	128

### E.2.3 Fine-tuning

For ADE20K fine-tuning, we add a single-block MaskTransformer decoder (Strudel et al., 2021) to the encoder. Both the encoder and decoder are fine-tuned end-to-end for 128 epochs with a batch size of 32, using the AdamW optimizer. Training hyperparameters are detailed in Table 12. The hyperparameters used, including learning rate, were selected on a prototyping model and not tuned for our final model(s) on which we report the final results.

Fine-tuning evaluation was performed using images at  $512 \times 512$  resolution. We interpolate the position embeddings to accommodate the processing of  $512 \times 512$  px images, a change which the model is quickly able to adapt to with fine-tuning.

For evaluation, images are simply resized to  $512 \times 512$ , with no other transformations applied.

Table 12: Hyperparameter configuration for ADE20K segmentation fine-tuning. Learning rate (LR) reference values are shown relative to a batch size of 256 and linearly scaled for the actual batch size (32).

Hyperparameter		ViT-S, -B	ViT-L
Encoder	Drop path	0.1	0.2
Decoder	Type	MaskTransformer	MaskTransformer
	Depth	1 block	1 block
Data	Input size	512	512
	Cropping	RandScale(0.5, 2.0)	RandScale(0.5, 2.0)
	HFlip	$p=0.5$	$p=0.5$
	Cutout	$p=0.5$	$p=0.5$
	ColorJitter	$p=0.5$	$p=0.5$
Training	Loss	CrossEntropy	CrossEntropy
	Optimizer	AdamW	AdamW
	LR schedule	Cosine	Cosine
	Warmup	10 epochs	10 epochs
	LR initial	0.0	0.0
	LR max (per 256 samp.)	$7.5 \times 10^{-3}$	$2.5 \times 10^{-3}$
	LR final	0.0	0.0
	LR layer decay	0.65	0.75
	Weight decay	0.05	0.05
	Batch size	32	32
	Epochs	128	128

## F Additional evaluations

### F.1 Variance across random seeds

We ran experiments with three different seeds for model initialization and dataloader to investigate the stability of our model’s performance and significance of the results. For this experiment, all models were trained for 300 epochs. As shown in Table 13, the differences between methods are significant, and Bootleg has much more consistency in its frozen probe performance than I-JEPA, indicating our training method is more stable.

Table 13: Variance under change in random seed. We trained MAE, I-JEPA, and Bootleg (final hparams) ViT-S models for 300 ep. on IN-1k with three random seeds for both init and dataloader. Results are shown as mean  $\pm$  stdev.

Method	IN-1k acc.			ADE20K mIoU		
	Patch	CLS	X-Blk	kNN	Lin	Blk
MAE	43.2 $\pm$ 0.2	35.9 $\pm$ 1.1	64.5 $\pm$ 0.0	9.6 $\pm$ 0.3	13.5 $\pm$ 0.2	26.8 $\pm$ 0.3
I-JEPA	51.5 $\pm$ 2.9	N/A	62.1 $\pm$ 2.3	9.0 $\pm$ 1.9	12.7 $\pm$ 2.2	22.4 $\pm$ 2.1
Bootleg (ours)	67.2 $\pm$ 0.6	68.3 $\pm$ 0.6	74.0 $\pm$ 0.3	21.8 $\pm$ 0.3	26.3 $\pm$ 0.3	33.8 $\pm$ 0.8

### F.2 Fine-tuned models

We fine-tuned SSL-pretrained models at IN-1k classification using fine-tuning on 100% of the training data (full fine-tuning), 1% of the data (low-shot, full fine-tuning), and 1% of the data using LoRA (low-shot, low-rank fine-tuning), as described in Appx. E.1.2. We additionally fine-tuned on ADE20K segmentation, as described in Appx. E.2.3.

**Results** As shown in Table 14, Bootleg achieves the best or near-best fine-tuning performance across all settings. On IN-1k 100% fine-tuning, Bootleg outperforms all baselines at every model size, with particularly large margins at ViT-S (+0.9 over the next best) and ViT-L (+0.7). The advantage is most pronounced in the low-data regime: on 1% fine-tuning, Bootleg surpasses the next-best method by +8.6 (ViT-B) and +12.5 (ViT-S) points, demonstrating that hidden-self-distillation produces representations that are especially effective when labelled data is scarce. LoRA fine-tuning follows a similar pattern, with Bootleg matching or exceeding full fine-tuning of I-JEPA despite updating far fewer parameters.

On ADE20K fine-tuning, Bootleg leads at ViT-S and ViT-B; at ViT-L, data2vec 2.0 and MAE are stronger.

Data2vec 2.0 full fine-tuning was sometimes unstable at the learning rates used for these experiments (collapsed

model at 0.1% acc.) and would benefit from a reduced learning rate.

Table 14: Fine-tuning results on IN-1k classification (top-1 accuracy, %) and ADE20K semantic segmentation (mIoU, %). IN-1k results include full fine-tuning on 100% and 1% of training data, and LoRA fine-tuning on 1%. Ep: number of pretraining epochs.

Arch	Method	Data	Ep.	IN-1k acc.			ADE20K mIoU
				Full-FT		LoRA	Full-FT
				100%	1%	1%	100%
ViT-S/16	MAE	IN-1k	800	78.2	37.1	33.9	39.2
	CrossMAE	IN-1k	800	79.8	40.4	37.5	<u>42.2</u>
	data2vec 2.0	IN-1k	200	79.9	39.3	36.8	40.5
	I-JEPA	IN-1k	600	<u>79.9</u>	<u>48.6</u>	<u>47.3</u>	36.1
	Bootleg (ours)	IN-1k	600	<b>80.8</b>	<b>61.1</b>	<b>60.4</b>	<b>44.3</b>
ViT-B/16	MAE	IN-1k	1600	82.7	55.9	53.5	44.0
	CrossMAE	IN-1k	800	82.9	52.3	49.6	<u>45.0</u>
	data2vec 2.0	IN-1k	200	<u>83.3</u>	58.9	58.1	0.1
	I-JEPA	IN-1k	600	82.7	<u>61.9</u>	<u>62.2</u>	29.8
	Bootleg (ours)	IN-1k	600	<b>83.9</b>	<b>70.5</b>	<b>69.9</b>	<b>46.6</b>
ViT-L/16	MAE	IN-1k	1600	<u>84.7</u>	67.7	67.5	<u>50.7</u>
	CrossMAE	IN-1k	800	84.3	62.7	61.7	49.6
	data2vec 2.0	IN-1k	200	0.1	<u>73.2</u>	<b>74.1</b>	<b>51.8</b>
	I-JEPA	IN-1k	600	82.0	63.8	63.8	31.9
	Bootleg (ours)	IN-1k	600	<b>85.4</b>	<b>73.4</b>	<u>73.2</u>	48.3

### F.3 VTAB classification

We evaluate on the Visual Task Adaptation Benchmark (VTAB) (Zhai et al., 2019), which comprises 19 diverse visual classification tasks grouped into three categories: Natural, 7 standard recognition tasks such as CIFAR-100, Caltech-101, and Flowers-102; Specialized, 4 domain-specific tasks including medical, satellite, and remote sensing imagery; and Structured, 8 tasks requiring geometric or spatial reasoning, such as object counting and orientation estimation.

#### F.3.1 Method.

Following the VTAB methodology, we train our probes for 50 epochs on a 1000 sample subset of the training set only, without data augmentation. We use the same probe types as for IN-1k (Patch, CLS, X-Blk), evaluated on the full test set.

The training hyperparameters (learning rate and weight decay) are selected by training a model on a subset of 800 training samples, validated on 200 samples. The best performing method is then trained again from scratch on the set 1000 training samples. The evaluation hyperparameters considered are shown in Table 15. Due to the diversity of the tasks, we needed a wider range of learning rate and weight decay hyperparameters to attain optimal results across the models and dataset pairs; consequently, we sweep an  $11 \times 11$  grid of learning rate and weight decay values for each head, using a wider spacing (factor of 3 spacing instead of 2):  $\eta_{\max} \in [3 \times 10^{-5}, 1.5 \times 10^{-4}, 3 \times 10^{-4}, \dots, 3.0]$   $\lambda \in [0, 1 \times 10^{-4}, 3 \times 10^{-4}, \dots, 3.0]$ .

#### F.3.2 Results.

Table 16 presents category-average results across Natural, Specialized, and Structured task groups. Among the non-contrastive methods, Bootleg achieves the highest overall accuracy across all three probe types at ViT-S and is best or second-best at ViT-B and ViT-L. The gains are most pronounced on Natural tasks, where Bootleg leads by a wide margin (e.g., 59.8% vs. 47.9% Patch at ViT-S), and on Specialized tasks, where Bootleg consistently achieves top scores. On Structured tasks, which require spatial reasoning and counting, CrossMAE and data2vec 2.0 are more competitive, likely due to their pixel-level reconstruction objectives. At ViT-L, Bootleg’s X-Blk probe achieves the highest overall accuracy (68.7%), with MAE and CrossMAE close behind on individual categories.

The contrastive baselines (DINOv2, Franca, CAPI), shown in gray, use a smaller patch size (ViT-S/14, ViT-B/14, ViT-L/14) which increases the effective sequence length and are trained on substantially larger curated datasets

Table 15: Hyperparameter configuration for VTAB frozen probes. We sweep an  $11 \times 11$  grid of learning rates and weight decay values for each probe type.

	Hyperparameter	Value
Encoder	Drop path	0.0
Data	Input size	$224 \times 224$
	Interpolation	Bicubic
	Auto-augment	None
Training	Loss	Cross-entropy
	Optimizer	AdamW
	LR schedule	Cosine decay
	Warmup	5 epochs
	LR initial	$2 \times 10^{-4}$
	LR max	$3 \times 10^{-5} \leq \eta_{\max} \leq 3.0$
	LR final	0.0
	WD	$0 \leq \lambda \leq 3.0$
	Batch size	64
	Epochs	50

(LVD-142M, LAION) and/or for significantly longer (CAPI is trained on IN-1k for ten times more epochs than Bootleg). Despite this advantage, Bootleg narrows the gap considerably on Natural and Specialized tasks.

A break-down of results on individual datasets is shown for the patch probe in Table 17.

Table 16: VTAB benchmark results: category-average top-1 accuracy (%) across Natural (7 tasks), Specialized (4 tasks), and Structured (8 tasks) categories. We report category-averages for Patch, CLS, and X-Blk frozen probes.

Arch	Method	Natural			Specialized			Structured			Overall		
		Patch	CLS	X-Blk									
ViT-S/16	MAE	45.7	46.2	57.6	76.6	<u>77.3</u>	78.2	39.1	<u>38.9</u>	53.2	49.5	49.7	60.1
	CrossMAE	<u>47.9</u>	<u>46.4</u>	<u>59.7</u>	<u>77.4</u>	76.0	<u>78.8</u>	<b>41.2</b>	<b>40.2</b>	<b>57.5</b>	<u>51.3</u>	<u>50.1</u>	<u>62.8</u>
	data2vec 2.0	38.8	37.4	48.4	74.6	75.6	74.1	40.1	38.4	<u>54.7</u>	46.9	45.8	56.5
	I-JEPA	40.2	N/A	45.8	74.3	N/A	73.8	37.7	N/A	43.9	46.3	N/A	50.9
	Bootleg (ours)	<b>59.8</b>	<b>59.8</b>	<b>66.2</b>	<b>79.0</b>	<b>78.1</b>	<b>80.8</b>	<u>40.4</u>	38.9	52.5	<b>55.6</b>	<b>54.9</b>	<b>63.5</b>
ViT-S/14	DINOv2 (dst)	<b>69.0</b>	<b>72.1</b>	<b>74.1</b>	<b>81.6</b>	<b>81.1</b>	<b>83.0</b>	39.3	36.4	57.7	59.1	59.0	69.1
ViT-B/16	MAE	54.3	53.4	64.4	76.7	<u>76.8</u>	79.2	42.2	42.2	<u>58.7</u>	53.9	53.6	65.1
	CrossMAE	<u>56.4</u>	<u>55.2</u>	<u>65.8</u>	<u>77.6</u>	74.3	<u>81.0</u>	<b>45.7</b>	<b>44.7</b>	<b>61.8</b>	<u>56.4</u>	<u>54.8</u>	<b>67.3</b>
	data2vec 2.0	52.6	43.9	54.6	76.6	71.6	72.4	<u>43.7</u>	<b>44.9</b>	53.8	53.9	50.2	58.0
	I-JEPA	50.4	N/A	55.1	77.2	N/A	78.5	39.8	N/A	49.8	51.6	N/A	57.8
	Bootleg (ours)	<b>60.7</b>	<b>61.5</b>	<b>68.0</b>	<b>82.1</b>	<b>80.5</b>	<b>83.7</b>	39.8	38.0	57.8	<b>56.4</b>	<b>55.6</b>	<u>67.0</u>
ViT-B/14	Franca	<u>66.5</u>	<u>71.3</u>	<u>75.1</u>	<u>82.1</u>	<u>79.7</u>	<u>83.3</u>	<u>38.6</u>	<u>32.8</u>	<u>57.3</u>	<u>58.1</u>	<u>56.9</u>	<u>69.3</u>
	DINOv2 (dst)	<b>72.8</b>	<b>74.6</b>	<b>78.1</b>	<b>83.1</b>	<b>81.7</b>	<b>84.2</b>	<b>41.3</b>	<b>37.2</b>	<b>58.3</b>	<b>61.8</b>	<b>60.3</b>	<b>71.1</b>
ViT-L/16	MAE	56.2	<u>60.1</u>	65.7	<u>79.4</u>	<u>80.2</u>	<u>81.6</u>	45.4	44.7	<u>62.1</u>	56.6	<b>57.9</b>	<u>67.5</u>
	CrossMAE	<u>59.1</u>	57.6	<u>68.4</u>	78.8	<b>80.5</b>	81.4	<u>46.0</u>	<u>46.5</u>	54.1	<b>57.7</b>	<u>57.8</u>	65.1
	data2vec 2.0	51.9	47.9	55.5	77.8	74.0	80.1	<b>46.3</b>	<b>46.5</b>	<b>62.5</b>	55.0	52.8	63.6
	I-JEPA	54.0	N/A	58.0	78.4	N/A	79.1	38.0	N/A	46.3	52.4	N/A	57.5
	Bootleg (ours)	<b>60.7</b>	<b>64.9</b>	<b>70.9</b>	<b>81.9</b>	79.7	<b>84.2</b>	41.5	39.7	58.9	<u>57.1</u>	57.4	<b>68.7</b>
ViT-L/14	CAPI	62.4	N/A	72.7	80.8	N/A	83.5	<b>44.9</b>	N/A	<b>63.1</b>	58.9	N/A	70.9
	Franca	<u>71.2</u>	<u>68.7</u>	<u>78.6</u>	<u>82.2</u>	<u>78.9</u>	<u>84.5</u>	38.9	<u>32.2</u>	<u>60.1</u>	<u>59.9</u>	<u>55.5</u>	<u>72.1</u>
	DINOv2 (dst)	<b>72.9</b>	<b>75.5</b>	<b>79.6</b>	<b>83.8</b>	<b>84.4</b>	<b>84.7</b>	<u>42.5</u>	<u>37.7</u>	57.0	<u>62.4</u>	<b>61.5</b>	<u>71.2</u>

Table 17: VTAB benchmark results: per-dataset top-1 accuracy (%) using the Patch (linear) frozen probe. C100 = CIFAR-100, Cal. = Caltech-101, Flr. = Flowers-102, Cam. = Camelyon17, Eur. = EuroSAT, Res. = Resisc45, Ret. = Retinopathy, Cl = Clevr, dS = dSprites, sN = SmallNORB, DM = DMLab, Kit. = KITTI. SOTA contrastive baselines (grey) use 14×14 patch sizes; non-contrastive (black) use 16×16.

Method	Natural							Specialized				Structured							
	C100	Cal.	DTD	Flr.	Pets	Sun	SVH	Cam.	Eur.	Res.	Ret.	Cl <sub>C</sub>	Cl <sub>D</sub>	dS <sub>L</sub>	dS <sub>O</sub>	sN <sub>A</sub>	sN <sub>E</sub>	DM	Kit.
<b>ViT-S</b>																			
MAE	24.1	74.1	54.0	65.3	35.6	18.4	48.6	76.3	90.8	65.7	73.8	42.4	46.4	44.0	31.0	18.5	39.4	33.6	57.7
CrossMAE	<u>26.6</u>	<u>76.4</u>	<u>54.4</u>	<u>68.3</u>	45.0	15.8	<u>48.8</u>	<b>78.9</b>	89.6	<u>67.2</u>	73.8	<u>47.8</u>	<u>50.6</u>	45.4	<b>34.5</b>	<b>19.6</b>	34.3	33.5	<b>63.9</b>
data2vec 2.0	20.3	59.9	47.1	60.4	24.4	15.2	44.3	73.5	88.1	63.4	73.5	44.3	<b>51.9</b>	<b>54.4</b>	18.9	16.5	<u>39.4</u>	<u>33.2</u>	62.0
I-JEPA	15.9	68.2	44.2	58.4	<u>46.1</u>	16.0	32.3	71.6	87.4	64.8	73.6	43.7	43.9	<u>53.4</u>	20.8	15.7	32.3	34.4	57.0
Bootleg (ours)	<b>35.8</b>	<b>87.4</b>	<b>62.9</b>	<b>80.2</b>	<b>70.9</b>	<b>32.0</b>	<b>49.1</b>	73.3	<b>92.3</b>	<b>75.9</b>	<b>74.4</b>	<b>49.5</b>	48.0	40.9	31.0	<u>18.9</u>	35.1	<b>36.2</b>	<u>63.4</u>
DINOv2 (dst)	54.1	89.1	74.1	97.4	77.9	46.6	43.6	82.0	91.0	78.3	75.0	48.7	48.7	34.3	38.2	19.5	32.3	35.2	57.7
<b>ViT-B</b>																			
MAE	27.1	<u>84.5</u>	<u>60.5</u>	73.8	62.7	<u>25.0</u>	46.4	<u>79.5</u>	90.2	<u>71.2</u>	65.8	<u>50.5</u>	48.5	43.8	<u>34.2</u>	20.3	36.8	<u>34.5</u>	<u>69.5</u>
CrossMAE	32.6	83.9	59.2	<u>75.1</u>	62.1	24.0	<u>57.7</u>	77.1	<u>90.8</u>	68.8	73.6	49.5	<u>52.6</u>	<u>48.8</u>	<b>46.2</b>	<b>24.5</b>	<b>39.5</b>	34.3	<b>70.6</b>
data2vec 2.0	<u>32.7</u>	80.3	56.1	66.3	44.6	24.1	<b>64.5</b>	75.2	90.2	67.0	73.9	<b>50.7</b>	<b>56.5</b>	<b>50.0</b>	29.0	<u>23.9</u>	37.6	32.6	69.1
I-JEPA	20.9	78.1	49.5	69.5	<b>78.9</b>	21.3	34.8	78.0	88.7	67.9	<u>74.1</u>	47.3	45.4	46.6	26.5	20.5	35.5	32.8	64.0
Bootleg (ours)	<b>35.1</b>	<b>87.8</b>	<b>64.0</b>	<b>82.7</b>	<u>75.2</u>	<b>34.9</b>	45.2	<b>82.4</b>	<b>92.5</b>	<b>78.5</b>	<b>74.9</b>	49.0	48.1	40.6	33.3	15.8	<u>39.0</u>	<b>36.0</b>	56.8
Franca	<u>49.6</u>	<u>87.2</u>	<u>72.5</u>	<u>94.8</u>	<u>71.5</u>	<u>42.9</u>	<u>47.0</u>	83.7	<u>91.7</u>	<u>77.8</u>	<u>75.4</u>	<u>48.8</u>	<u>49.2</u>	<u>35.7</u>	<u>36.0</u>	<u>14.8</u>	<u>33.0</u>	<u>36.2</u>	<u>55.4</u>
DINOv2 (dst)	<b>63.0</b>	<b>91.1</b>	<b>78.5</b>	<b>97.9</b>	<b>81.3</b>	<b>52.7</b>	<u>45.5</u>	<u>82.5</u>	<u>91.6</u>	<b>82.8</b>	75.6	49.4	<u>48.8</u>	<u>34.2</u>	<b>44.1</b>	17.5	34.3	41.2	<b>61.3</b>
<b>ViT-L</b>																			
MAE	28.5	84.8	<u>62.7</u>	75.5	62.3	26.4	53.5	<u>80.7</u>	91.1	<u>72.9</u>	73.0	52.6	49.9	48.1	<u>43.4</u>	23.8	39.5	34.5	<b>71.6</b>
CrossMAE	36.4	85.5	<b>63.0</b>	<u>76.5</u>	66.6	27.5	<b>58.0</b>	<b>81.6</b>	91.8	68.3	73.4	<u>52.8</u>	<u>50.3</u>	<b>51.9</b>	<b>49.4</b>	<u>24.0</u>	39.8	33.2	66.4
data2vec 2.0	<u>37.5</u>	82.4	54.0	67.3	41.8	23.0	<u>57.8</u>	80.2	90.3	69.7	71.0	<b>57.3</b>	<b>51.3</b>	<u>50.2</u>	38.4	<b>24.7</b>	<b>44.4</b>	<u>36.5</u>	<u>67.8</u>
I-JEPA	29.4	78.9	54.1	69.6	<b>78.8</b>	<u>28.1</u>	39.5	76.6	<u>91.9</u>	71.6	<u>73.5</u>	43.6	46.0	44.8	25.3	20.0	34.2	33.1	57.0
Bootleg (ours)	<b>39.2</b>	<b>88.0</b>	58.8	<b>85.1</b>	<u>69.5</u>	<b>34.5</b>	49.9	78.8	<b>92.8</b>	<b>80.9</b>	<b>75.2</b>	49.0	50.1	43.2	34.8	20.8	38.6	<b>37.2</b>	58.4
CAPI	42.3	86.3	69.3	84.6	62.0	38.0	54.6	77.9	<u>92.4</u>	78.1	<u>75.0</u>	<u>51.5</u>	<b>49.5</b>	41.4	37.1	<u>18.9</u>	50.2	37.5	73.6
Franca	<u>64.9</u>	<b>90.7</b>	<u>72.6</u>	<u>98.0</u>	<u>80.4</u>	<u>48.4</u>	<u>43.2</u>	<u>81.1</u>	91.0	<u>80.3</u>	<u>76.2</u>	43.5	<u>49.3</u>	<u>36.1</u>	<b>44.1</b>	<b>19.2</b>	<u>34.5</u>	<u>40.5</u>	44.6
DINOv2 (dst)	<b>69.0</b>	<u>90.7</u>	<b>78.1</b>	<b>99.0</b>	<b>82.1</b>	<b>50.0</b>	41.2	83.7	<b>92.5</b>	<b>86.1</b>	73.0	52.7	48.6	36.0	<u>43.5</u>	18.3	33.6	<b>42.1</b>	<u>64.8</u>

## G Additional ablations

### G.1 Preliminary hyperparameters

As described in Appx. B, our hyperparameter sweep was conducted in multiple rounds. Some ablations were conducted using a prototype hyperparameter configuration, before the final hyperparameters were established. The prototype and final configurations are compared in Table 18.

Additionally, note that tables using prototype hyperparameter values use a weaker implementation of the IN-1k probe methodology (too large a range in crop sizes, too small a range in LR values), and are not comparable with the main tables but are self-consistent.

Table 18: Preliminary and final ablation hyperparameter configurations, each used for some of the ablation experiments presented (ViT-S, 300 ep.).

	Hyperparameter	Bootleg (prototype)	Bootleg (final)
Encoder	Architecture	ViT-S/16	ViT-S/16
	Depth	12	12
	Width	384	384
	Attention heads	6	6
	Patch size	16	16
	CLS tokens	1	1
	Register tokens	4	4
Predictor	Depth	8	10
	Width	256	192
	Attention heads	8	16
	Register tokens	4	4
Data	Transforms	RandCrop(0.2, 1.0) + Hflip	RandCrop(0.35, 1.0) + Hflip
	Interpolation	Bicubic	Bicubic
	Input size	224×224	224×224
Masking	Strategy	4 rectangular blocks	4 rectangular blocks
	Mask seen rate	0.292 ± 0.069	0.292 ± 0.069
	Mask target rate	0.475 ± 0.076	0.475 ± 0.076
Training	Target(s)	Block 1, 4, 8, 12 outputs	Block 1, 4, 8, 12 outputs
	Target standardization	Z-score	Z-score
	Target length	1536	1536
	Loss	Mean squared error	Mean squared error
	Optimizer	AdamW( $\beta=(0.9, 0.95)$ )	AdamW( $\beta=(0.9, 0.95)$ )
	EMA initial	0.998	0.9985
	EMA final	1.0	0.9985
	LR schedule	Cosine annealing	Cosine annealing
	LR schedule warmup	40 epochs	69 epochs
	LR initial	0.0	0.0001
	LR maximum	0.0012	0.003
	LR final	0.0	0.0001
	WD initial	0.05	0.05
	WD final	0.05	0.05
Schedule stretch	1.25	1.0	
Batch size	2048	2048	
Num epochs	300	300	

### G.2 Choice of target layers

To accompany Sec. 6.1, we show additional results exploring which hidden layers to use as targets for hidden-self-distillation.

#### G.2.1 Number of targets.

As shown in Table 19, we explore the effect of varying how many hidden layers are targeted for self-distillation, the type of intermediate representation used (block outputs, mid-block representations, residual terms), and whether to include the tokenizer output or raw image pixels. For ViT-S, we find two peaks in performance: one when using 3–4 equispaced block outputs as targets, and another when targeting all residuals and outputs

from every block. For ViT-B and ViT-L, the equispaced block outputs consistently outperform the denser target configurations. Overall, targeting the output of every fourth block provides best or near-best performance across all three architecture sizes.

Table 19: Selection of which hidden layer(s) to predict during pretraining. Block sets are denoted start : step : end, e.g., 1 : 4 : 12 = {1, 4, 8, 12} and 1 : 1 : 12 denotes all blocks. Experiments trained for 300 ep. on IN-1k (using *prototype* hparams) and evaluated with frozen probe. We also show the number of distillation targets per mask token. We find using the output of every fourth block (highlighted) provides best or near best performance across architecture sizes.

Arch	Targets	# Distillation targets			IN-1k Probe		
		Blocks	Layers	Dim	Patch	CLS	X-Blk
ViT-S	Block 12 output	1	1	384	54.1	53.8	68.5
	Block 1:6:12 output	3	3	1152	<b>62.9</b>	<b>62.8</b>	72.5
	Block 1:4:12 output	4	4	1536	62.2	62.4	<b>73.0</b>
	Block 1:3:12 output	5	5	1920	60.7	61.3	72.8
	Block 2:2:12 output	6	6	2304	59.8	61.5	72.8
	Block 1:4:12 output and residuals	4	12	4608	57.6	54.3	70.2
	Block 1:1:12 output	12	12	4608	58.5	56.3	72.2
	Block 1:1:12 residuals	12	24	9216	55.6	54.8	70.0
	Block 1:1:12 mid and output	12	24	9216	59.3	59.9	72.8
	Block 1:1:12 residuals and output	12	36	13824	<u>62.4</u>	61.9	<b>73.1</b>
	Block 1:1:12 residuals, mid, output	12	48	18432	61.7	<b>63.1</b>	<u>73.0</u>
	Img; Tok; Block 1:1:12 res., mid, output	2+12	50	19584	60.5	61.7	72.9
ViT-B	Block 1:6:12 output	3	3	2304	<u>72.3</u>	<u>73.4</u>	78.2
	Block 1:4:12 output	4	4	3072	<b>73.4</b>	<b>74.4</b>	<b>78.7</b>
	Block 1:3:12 output	5	5	3840	72.1	71.7	<u>78.3</u>
	Block 1:2:12 output	6	6	4608	70.2	70.8	78.0
	Block 1:1:12 output	12	12	9216	70.4	68.2	77.7
	Block 1:1:12 residuals and output	12	36	27648	70.3	70.7	77.8
ViT-L	Block 1:8:24 output	4	4	4096	<b>77.9</b>	<u>77.4</u>	<u>81.2</u>
	Block 1:4:24 output	7	7	7168	<u>77.9</u>	<b>78.0</b>	<b>81.2</b>
	Block 1:1:24 residuals and output	24	72	73728	77.1	76.1	80.8

### G.2.2 Whether to use the tokenizer block.

We considered whether to include the tokenizer, the least processed layer after the raw image pixels, as a self-distillation target. This layer’s output has an advantage over the raw image pixels in being the same shape as the transformer block outputs, which (though not strictly necessary) does make processing easier. As shown in Table 20, we found using the tokenizer’s output instead of the first block when using spaced out targets was detrimental. For target configurations where all transformer blocks were being predicted, including the tokenizer layer as a self-distillation target was generally negative on IN-1k performance.

Table 20: Choosing whether to predict the tokenizer’s output. We consider whether to predict the tokenizer output (Tok.) instead of the first block for spaced targets, or in addition to all blocks. We find it is generally disadvantageous to use the tokenizer as a self-distillation target in these scenarios. ViT-S, trained on IN-1k, 300 ep., *prototype* hparams.

Distillation targets	# tgt	IN-1k Probe		
	Layer	Patch	CLS	X-Blk
Block 1:4:12 out	4	<u>62.2</u>	<b>62.4</b>	<u>73.0</u>
Block 4:4:12 out & Tok.	4	60.3	61.6	72.4
Block 1:1:12 out	12	58.5	56.3	72.2
Block 1:1:12 out & Tok.	13	59.2	59.2	72.4
Block 1:1:12 mid, out	24	59.3	59.9	72.8
Block 1:1:12 mid, out & Tok.	25	58.9	58.9	72.3
Block 1:1:12 res., out	36	<b>62.4</b>	<u>61.9</u>	<b>73.1</b>
Block 1:1:12 res., out & Tok.	37	60.4	58.7	72.5

### G.3 Masking hyperparameter sensitivity

We ablate the masking hyperparameters of Bootleg: the size of each mask region (Table 21), the number of mask regions (Table 22), and the aspect ratio range of mask regions (Table 23).

For each ablation, we report the average fraction of patch tokens which were seen by the encoder, and the fraction of patch tokens used as a target by at least one mask. We also show the fraction of targets which were adjacent to a seen token.

#### G.3.1 Mask size

Table 21 shows the effect of scaling mask region size while keeping  $K=4$  regions fixed. The default mask scale (100%) yields the best results across all metrics. The performance falls off similarly as the mask size is increased or decreased. Smaller masks (80%) leave too much context visible (40.3% seen), reducing the difficulty of the prediction task, while larger masks (110–120%) occlude too much of the image, limiting the encoder’s access to informative context. Performance holds out well across the range of mask sizes explored, despite the mean seen rate ranging from 22% to 40%.

Table 21: Effect of mask region size. The mask scale is varied as a percentage relative to the default (highlighted), keeping the number of mask regions fixed at  $K=4$ . ViT-S, 300 ep. on IN-1k.

K	Mask scale	Seen (%)	Target (%)	Adj. (%)	IN-1k acc.			ADE20K mIoU
					Patch	CLS	X-Blk	kNN
4	80% → [0.128, 0.146]	40.3 ± 7.7	40.6 ± 6.4	27.8 ± 10.2	65.3	64.9	73.2	19.7
4	90% → [0.144, 0.165]	33.9 ± 7.1	44.5 ± 7.0	21.7 ± 9.2	<u>67.2</u>	<u>68.3</u>	<u>74.2</u>	21.1
4	100% → [0.160, 0.183]	29.3 ± 6.7	47.3 ± 7.3	17.7 ± 8.3	<b>67.8</b>	<b>68.9</b>	<b>74.4</b>	<b>22.0</b>
4	110% → [0.176, 0.201]	25.5 ± 6.4	49.7 ± 7.6	14.5 ± 7.5	66.7	67.7	73.6	<u>21.7</u>
4	120% → [0.192, 0.220]	21.8 ± 6.4	52.2 ± 8.0	11.6 ± 6.8	65.1	66.2	73.1	21.2

#### G.3.2 Number of masks

Table 22 varies the number of mask regions,  $K$ , while adjusting their size to keep the total masked area approximately constant. The default  $K=4$  achieves the best results, with  $K=3$  and  $K=5$  close behind. Fewer, larger masks ( $K=1$ ,  $K=2$ ) produce contiguous masked regions that occlude a large area, elevating the task. Many small masks ( $K=8$ ) scatter targets across the image, reducing task difficulty slightly due to the reduced size of each mask. The results suggest that a moderate number of mask regions provides the best balance between prediction difficulty and spatial diversity. Performance holds out well across the range of number of mask regions.

Table 22: Effect of changing the number of mask regions,  $K$ . The mask scale is adjusted to keep the seen fraction of the image approximately constant. The mask scale percentage is relative to the default ( $K=4$ ). ViT-S, 300 ep. on IN-1k.

K	Mask scale	Seen (%)	Target (%)	Adj. (%)	IN-1k acc.			ADE20K mIoU
					Patch	CLS	X-Blk	kNN
1	379% → [0.575, 0.726]	28.4 ± 8.0	64.8 ± 5.0	19.5 ± 7.1	67.2	67.5	73.5	21.2
2	208% → [0.281, 0.432]	29.1 ± 7.7	52.0 ± 8.0	16.1 ± 7.0	67.1	67.6	73.6	21.4
3	131% → [0.196, 0.254]	28.7 ± 7.2	47.3 ± 7.8	16.0 ± 8.0	<u>67.5</u>	<u>68.6</u>	74.0	21.7
4	100% → [0.160, 0.183]	29.3 ± 6.7	47.3 ± 7.3	17.7 ± 8.3	<b>67.8</b>	<b>68.9</b>	<b>74.4</b>	<b>22.0</b>
5	86% → [0.126, 0.168]	28.6 ± 7.4	48.9 ± 7.6	18.2 ± 9.0	67.3	68.1	<u>74.1</u>	<u>21.8</u>
6	72% → [0.109, 0.138]	30.0 ± 6.9	48.9 ± 7.1	20.8 ± 9.1	66.9	67.7	73.8	21.1
8	57% → [0.083, 0.111]	29.2 ± 7.0	50.8 ± 6.9	22.1 ± 9.6	65.5	66.1	73.5	20.4

#### G.3.3 Mask aspect ratio

Table 23 compares different aspect ratio ranges for mask regions. The default range [0.667, 1.5] achieves the best performance across all metrics. There is only a small impact on the performance of the model when changing the mask aspect ratio.

Using square masks slightly increases the difficulty in the task because more targets are further from seen components of the image. Similarly, wider aspect ratio ranges ([0.5, 2] and [0.333, 3]) increases the task difficulty

slightly as highly elongated mask rectangles allow the model to see context closer to the target patches. The default aspect ratio provides the best balance in task complexity, though the effect is not large.

Table 23: Effect of mask aspect ratio range. The default aspect ratio (highlighted) allows moderate variation; [1, 1] constrains masks to be square. ViT-S,  $K=4$ , 300 ep. on IN-1k. Although the mask scale parameter is held constant, the seen rate varies due to changes in the distribution of possible mask areas for a given aspect ratio range.

Aspect ratio	Seen (%)	Target (%)	Adj. (%)	IN-1k acc.			ADE20K mIoU
				Patch	CLS	X-Blk	kNN
[1, 1]	25.1 ± 5.6	49.4 ± 7.5	14.0 ± 7.0	<u>67.2</u>	68.0	73.6	21.5
[0.667, 1.5]	29.3 ± 6.7	47.3 ± 7.3	17.7 ± 8.3	<b>67.8</b>	<b>68.9</b>	<b>74.4</b>	<b>22.0</b>
[0.5, 2]	30.1 ± 6.9	47.2 ± 7.2	18.8 ± 8.8	67.2	<u>68.3</u>	<u>74.2</u>	<u>21.6</u>
[0.333, 3]	30.4 ± 7.0	47.8 ± 7.2	19.8 ± 9.4	67.1	<u>67.7</u>	73.9	21.3

## H Additional experiments

In this section, we present additional experiments exploring design choices in the Bootleg framework. Unless otherwise noted, experiments use ViT-S pretrained on IN-1k for 300 epochs with the final hyperparameter configuration (Table 18).

### H.1 Predicting register tokens

In Bootleg, the embedding of the CLS token is passed from the encoder to the predictor, along with embeddings of the visible patches. However, the register tokens are not passed from the encoder to predictor. Instead, the predictor has its own register tokens.

Since the register tokens are not visible to the predictor, estimating these would be non-trivial for the predictor. We explored whether including the hidden embeddings of the register tokens as targets (in addition to the hidden-layer embeddings of the masked-out tokens) would improve the performance of the network. As shown in Table 24, we found including register tokens as targets has negligible impact in training performance.

Table 24: Effect of using hidden embeddings of register tokens as self-distillation targets, in addition to hidden embeddings of patch tokens. ViT-S, trained 300ep on IN-1k, *prototype* hparams.

Arch	Distil. method	IN-1k Probe			
		Patch	CLS	X-Attn	X-Blk
ViT-S	Baseline	<b>62.2</b>	<u>62.4</u>	<b>71.1</b>	<b>73.0</b>
	+target 4 reg.	<u>62.2</u>	<b>62.5</b>	<u>70.9</u>	<u>72.7</u>

Table 25: Effect of splitting targets across mask rectangles. We show the number of target layers per mask rectangle (/) and over all masks ( $\Sigma$ ). ViT-S, trained 300ep on IN-1k, *prototype* hparams.

Grouping method	Distillation targets per mask rectangle	# targets		IN-1k Probe			
		/	$\Sigma$	Patch	CLS	X-Attn	X-Blk
Same (all) for each rectangle	Blocks {1, 4, 8, 12} outputs	4	4	<u>62.2</u>	<b>62.4</b>	<u>71.1</u>	<u>73.0</u>
Split as single target per rect.	Block $g$ out; for $g = 1, 4, 8, 12$	1	4	60.7	61.7	70.8	72.7
Same (all) for each rectangle	Blocks 1:1:12 res. & out	36	36	<b>62.4</b>	<u>61.9</u>	<b>71.4</b>	<b>73.1</b>
Split as contiguous blocks	Blocks $\{g, g + 1, g + 2\}$ res. & out; for $g = 1, 4, 7, 10$	12	36	60.2	60.3	70.9	72.7
Split as interleaved blocks	Blocks $\{g, g + 4, g + 8\}$ res. & out; for $g = 1, 2, 3, 4$	12	36	60.7	57.9	70.5	72.6
Split as interleaved targets	$\{r_l^{\text{Attn}}, r_{l+1}^{\text{MLP}}, x_{l+2}\}$ for $l \in [1, 5, 9], \text{etc.}$	12	36	60.9	60.6	70.9	72.8

### H.2 Using different targets for each mask

To train ViT-S and ViT-B, our Bootleg method uses four self-distillation targets (the outputs of the teacher’s blocks 1, 4, 8, and 12), and predicts these targets for all masked out tokens within four blocking mask rectangles. Each rectangle is processed separately with self-attention between the encoder outputs and the mask tokens.

This symmetry presents an opportunity: what if we break up the distillation targets and ask the predictor to predict only a quarter of the hidden layers for each pass through the predictor? In the standard Bootleg config, this means each mask rectangle can devote its processing to predicting a single distillation target. Intuitively, this may yield an advantage if the predictor is “overloaded” in its capacity to predict all the targets.

We implemented this variant of Bootleg by using a different learnable mask token for each of the four mask regions. Since mask placement is symmetric, we let the first mask rectangle correspond to the first mask token and let its targets always be the output of block 1; similarly the second mask rectangle always predicts the output of block 4; *etc.* We retain the full dimensionality of the read-out head (the final linear layer of the predictor network) as if the module were predicting all four targets, but select only the dimensions corresponding to the  $i$ -th target; we found this was necessary to best facilitate the training of the predictor. As shown in Table 25, we found splitting up the target layers across the mask rectangles lead to a slight reduction in performance.

We also experimented with this method when using 36 targets: the output and residuals of each block. As this is a much larger set of targets, it is more likely the predictor is “overloaded” when trying to complete all prediction tasks simultaneously. For this set of targets, we explored multiple options of how to group the 36 targets into 4 sets of 12: (1) predict all 36 targets for every rectangle (default); (2) group blocks contiguously as  $\{1, 2, 3\}$ ,  $\{4, 5, 6\}$ ,  $\{7, 8, 9\}$ ,  $\{10, 11, 12\}$ ; (3) use interleaved blocks  $\{1, 5, 9\}$ ,  $\{2, 6, 10\}$ ,  $\{3, 7, 11\}$ ,  $\{4, 8, 12\}$ ; or (4) interleave targets entirely  $\{r_1^{\text{Attn}}, r_2^{\text{MLP}}, x_3, r_5^{\text{Attn}}, r_6^{\text{MLP}}, x_7, r_9^{\text{Attn}}, r_{10}^{\text{MLP}}, x_{11}\}$ ,  $\{r_1^{\text{MLP}}, x_2, r_4^{\text{Attn}}, r_5^{\text{MLP}}, x_6, r_8^{\text{Attn}}, r_9^{\text{MLP}}, x_{10}, r_{12}^{\text{Attn}}\}$ , *etc.* In this case, we found (Table 25) using all targets for each of the 4 rectangles worked best, followed by interleaving the targets as much as possible.

These results indicate that using every hidden distillation as a target for every masked out token is the superior strategy.

### H.3 Using a cross-attention predictor with Bootleg

To accompany the “Bootleg edition of CrossMAE” in Sec. 6.2, we considered whether Bootleg itself would perform better when using the cross-attention predictor of CrossMAE instead of a self-attention predictor network. As shown in Table 26, we found the using the cross-attention predictor on the output of the encoder only (XA without WFM) greatly reduced performance ( $62.4 \rightarrow 54.7$  patch probe). Using cross-attention with the weighted feature map (XA with WFM) was overall slightly worse than using self-attention. However, we did not increase the depth of the predictor network, as recommended by Fu et al. (2025); it is possible doing so would improve the results when training Bootleg with a cross-attention predictor.

Table 26: Performance when using cross-attention predictor and weighted feature map (CrossMAE config) instead of self-attention (MAE config). Performance when using either the MAE/I-JEPA method of self-attention (SA) for the predictor network, or the CrossMAE method of cross-attention (XA) against a weighted feature map (WFM). The WFM uses a learnable weighted average of the outputs from the tokenizer and outputs of each transformer block in the encoder as the input to the predictor. ViT-S, 300 ep., *prototype* hparams.

Arch	Distillation targets	Predictor	IN-1k Probe		
			Patch	CLS	X-Blk
ViT-S	Block 1:4:12 out	SA	62.2	<b>62.4</b>	<b>73.0</b>
	Block 1:4:12 out	XA, WFM	62.2	61.1	72.8
	Block 1:1:12 res., out	SA	<u>62.4</u>	<u>61.9</u>	<b>73.1</b>
	Block 1:1:12 res., out	XA	54.7	46.5	69.7
	Block 1:1:12 res., out	XA, WFM	<b>62.6</b>	59.1	72.6
ViT-B	Block 1:4:12 out	SA	<b>73.4</b>	<b>74.4</b>	<b>78.7</b>
	Block 1:4:12 out	XA, WFM	<u>72.9</u>	<u>72.6</u>	<u>78.7</u>

### H.4 Jointly standardizing targets

In Bootleg, our targets are standardized on a per-patch, per-hidden-layer basis by subtracting the mean and dividing by the standard deviation as measured over the embedding dimension (taking the z-score over the embedding dimension). This standardization process is the same as in I-JEPA (which only targets one layer, the output of the teacher-encoder), and originates in MAE (He et al., 2022), in which analysis found using the z-score of the RGB values, referred to as the “normalized pixel values”, was a better training target than the raw RGB values.

In self-distillation literature (Grill et al., 2020; Chen & He, 2021; Assran et al., 2023) taking the z-score of the targets—often as a z-score over the batch dimension, implemented by applying a BatchNorm module without an affine-transformation—is motivated by the need to prevent collapse of the representations. This representation collapse can be seen to motivate our own target standardization, but in this case it would be sufficient to standardize the full target vector, rather than standardizing each embedding vector.

We investigated this by considering two options to handle the preparation of the target vector for a given mask patch token: (1) first separately standardize each embedding vector from blocks 1, 4, 8, 12; then concatenate the standardized embeddings to create the target vector; (2) first concatenate the embedding vectors from blocks 1, 4, 8, 12; then jointly standardize the concatenated embedding vector. As shown in Table 27, we find separate standardization outperforms jointly standardizing the embeddings, though joint standardization does not result in a collapse in the model.

Table 27: We explored whether to standardize the targets with a z-score separately applied to each target embedding vector from each hidden layer used, or with a z-score taken across the concatenation of all targets. ViT-S, trained on IN-1k, 300 ep. *prototype* hparams.

Target standardization	# targets	IN-1k Probe		
	Layers	Patch	CLS	X-Blk
Separately standardized	4	<b>62.2</b>	<b>62.4</b>	<b>73.0</b>
Jointly standardized	4	57.8	57.2	69.8

## I Representational analysis

To better understand the structure of Bootleg’s learned representations, we analyze how embeddings relate across transformer blocks and spatial positions. We compute two inter-layer similarity measures—element-wise Pearson correlation and Centered Kernel Alignment (CKA) Kornblith et al. (2019)—as well as spatial autocorrelation within each layer. All analyses are computed over 10,000 ImageNet-1k validation images using ViT-S/16 and ViT-B/16 Bootleg encoders trained for 600 epochs.

### I.1 Inter-layer similarity

Fig. 6 shows Pearson correlation matrices between all pairs of encoder layers (tokenizer output, blocks 1–12, and the final layer-normed output used as I-JEPA’s target). Several patterns emerge. Adjacent layers are highly correlated (mean adjacent Pearson  $r = 0.81$  for ViT-S, 0.84 for ViT-B), but correlation decays rapidly with layer distance, reaching near-zero between early and late blocks. Block 12’s output is notably distinct from earlier layers, with Pearson  $r < 0.10$  against blocks 1–4 in ViT-S. The “final” representation (post-LayerNorm) shows moderate correlation with late blocks but low correlation with early blocks, confirming that it is dominated by the deepest layers.

Fig. 7 shows the corresponding CKA matrices. CKA values are systematically higher than Pearson correlations for distant layer pairs (e.g., CKA between tokenizer and final is 0.58 for ViT-S vs. Pearson  $r = 0.05$ ), reflecting CKA’s sensitivity to shared geometric structure even when per-element correspondence is weak. Despite this scale difference, CKA and Pearson rankings are strongly correlated ( $\rho = 0.89$  for both architectures; Fig. 8).

### I.2 Distillation target layer analysis

Bootleg uses blocks 1, 4, 8, and 12 as distillation targets. Fig. 9 shows how each layer’s representation correlates with these four targets. Each target block correlates most strongly with its immediate neighbors and has a peaked profile, confirming that the targets sample distinct regions of the representation space. The early target (block 1) and late target (block 12) are particularly dissimilar (Pearson  $r < 0.06$  for ViT-S), supporting the hypothesis that multi-layer targets provide complementary training signal spanning low-level and semantic features.

### I.3 Spatial correlation structure

We also analyze how patch embeddings within a single layer correlate as a function of their spatial separation. For each layer, we compute the Pearson correlation between all pairs of patch tokens at a given spatial offset ( $\Delta r, \Delta c$ ) and average over images.

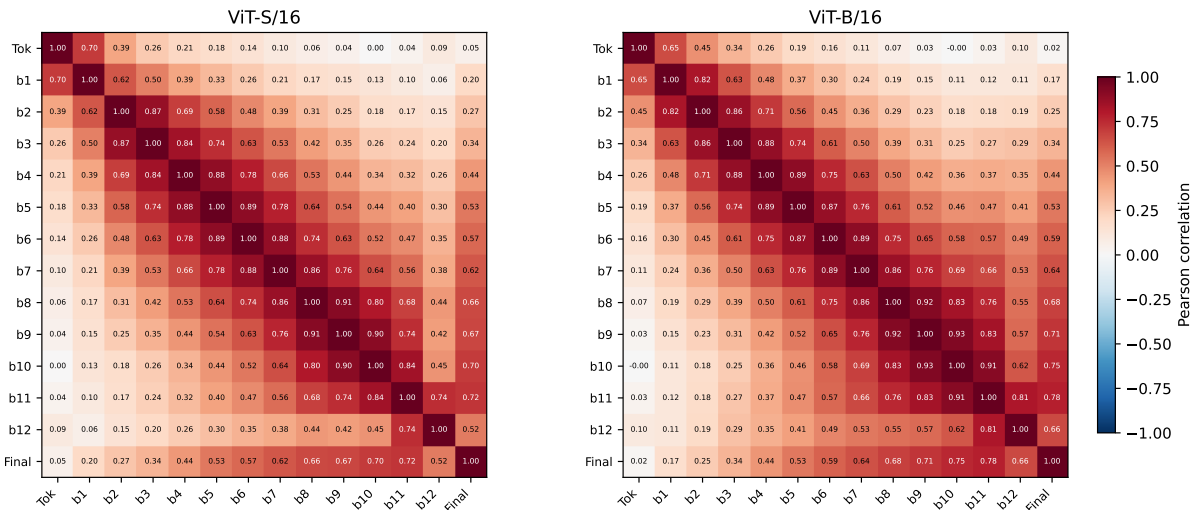


Figure 6: Inter-layer Pearson correlation matrices for Bootleg ViT-S/16 and ViT-B/16 encoders. Each cell shows the mean correlation between embedding vectors at corresponding spatial positions across 10,000 images. Correlation decays with layer distance, and the final block is highly distinct from early blocks.

Fig. 10 shows the azimuthally averaged spatial correlation as a function of distance (in patch units). In early layers, spatial correlation decays steeply—nearby patches are moderately correlated but distant patches are nearly independent. In the deepest block (block 12), spatial correlations are uniformly high (global mean 0.76 for ViT-S, 0.61 for ViT-B), reflecting the emergence of a global, spatially uniform representation. The final LayerNorm output partially reverses this effect, lowering the global mean correlation and restoring some spatial structure. Across all layers, ViT-B shows slightly lower spatial correlations than ViT-S, consistent with the larger model retaining more spatially-specific information.

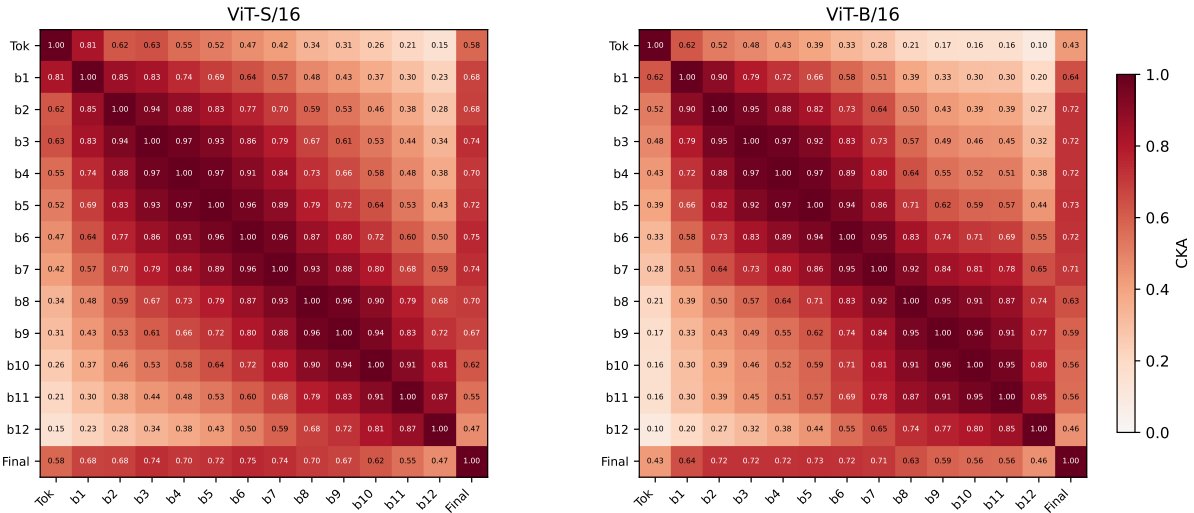


Figure 7: Inter-layer CKA similarity matrices. CKA captures shared representational geometry and yields higher values than Pearson correlation for distant layer pairs, but the two measures are strongly rank-correlated ( $\rho \approx 0.89$ ).

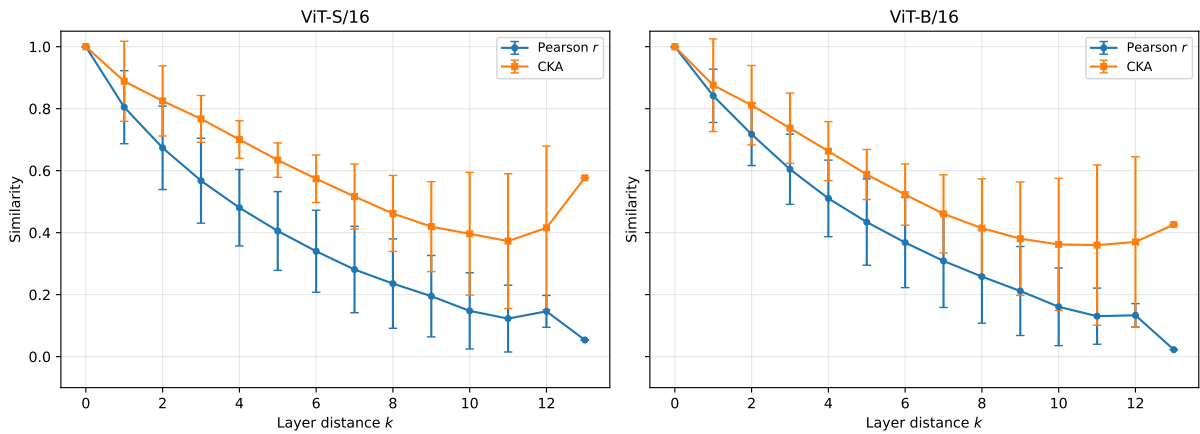


Figure 8: Off-diagonal decay of Pearson correlation and CKA as a function of layer distance  $k$ . CKA decays more slowly, remaining above 0.15 even at the maximum distance, while Pearson correlation drops near zero. Error bars show standard deviation across all layer pairs at each distance.

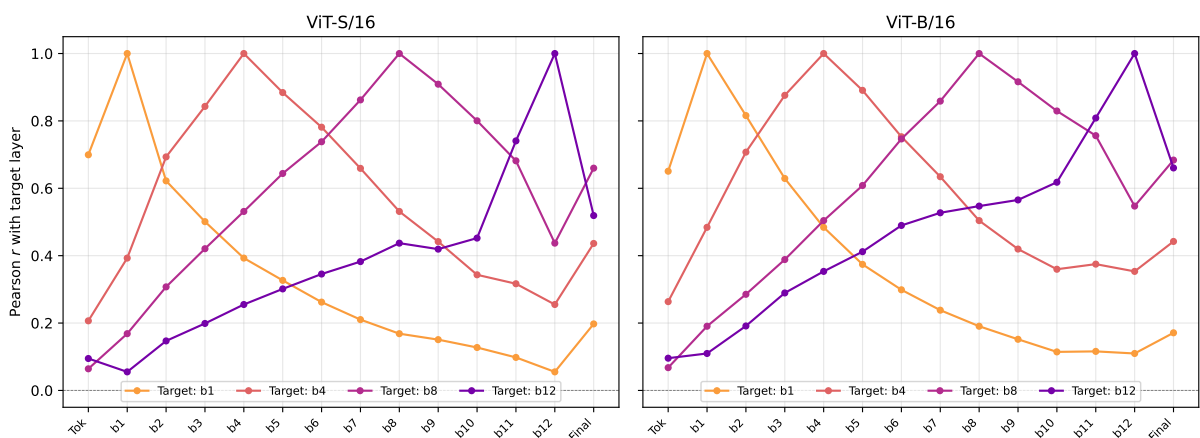


Figure 9: Pearson correlation of each encoder layer with the four Bootleg distillation target layers (blocks 1, 4, 8, and 12). Each target’s profile peaks at its own block and decays with distance, confirming that the targets capture non-redundant representations.

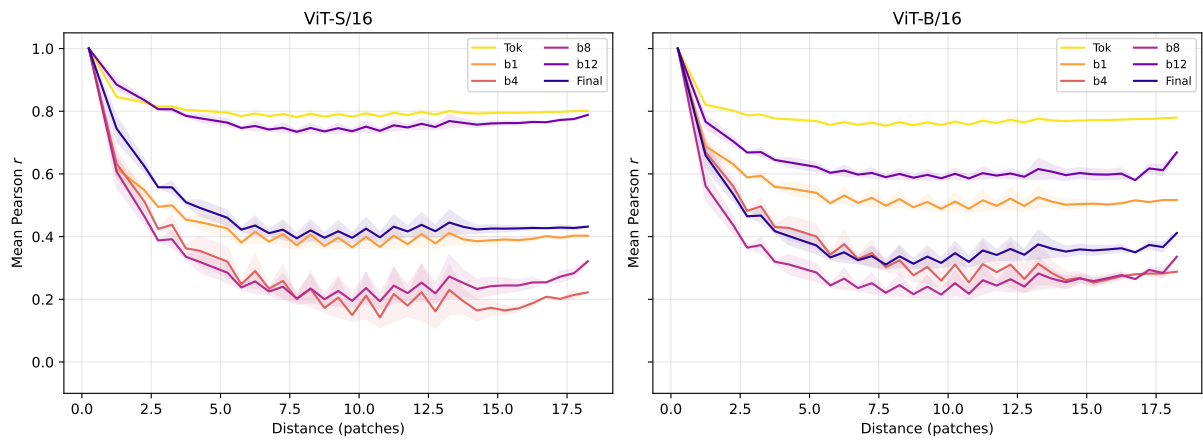


Figure 10: Azimuthally averaged spatial correlation vs. distance for selected encoder layers. Early layers exhibit localized correlations that decay with distance. Block 12 shows near-uniform high correlation, indicating a globally coherent representation. The post-LayerNorm final output partially restores spatial structure.